iScience

CellPress
OPEN ACCESS

Article

Nyquist-exceeding high voxel rate acquisition in mesoscopic multiphoton microscopy for full-field submicron resolution resolvability

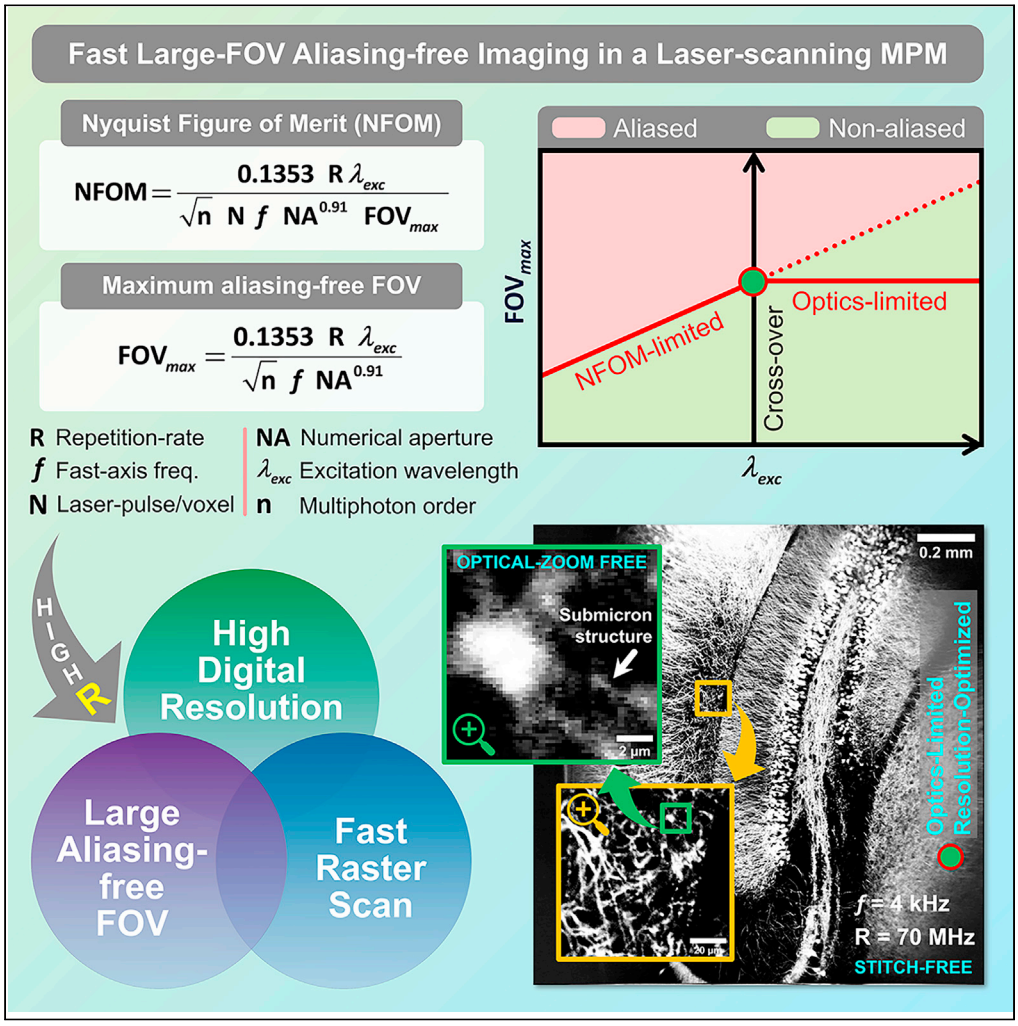

Bhaskar Jyoti Borah, Jye-Chang Lee, Han-Hsiung Chi, Yang-Ting Hsiao, Chen-Tung Yen, Chi-Kuang Sun

sun@ntu.edu.tw

Highlights

Nyquist figure-of-merit is introduced to characterize laser-scanning MPM digitization

Maximum aliasing-free FOV and cross-over excitation wavelength are formulated

High repetition-rate laser can enable high-speed large-FOV high-resolution MPM imaging

Up-to 1.6 mm-wide non-aliased FOV and ~400 nm digital resolution at 8 kHz line-rate

Borah et al., iScience 24, 103041
September 24, 2021
https://doi.org/10.1016/j.isci.2021.103041

iScience

CellPress
OPEN ACCESS

Article

Nyquist-exceeding high voxel rate acquisition in mesoscopic multiphoton microscopy for full-field submicron resolution resolvability

Bhaskar Jyoti Borah,[1] Jye-Chang Lee,[2] Han-Hsiung Chi,[2] Yang-Ting Hsiao,[1] Chen-Tung Yen,[2] and Chi-Kuang Sun[1,3,4,5,*]

SUMMARY

The Nyquist-Shannon criterion has never been realized in a laser-scanning mesoscopic multiphoton microscope (MPM) with a large field-of-view (FOV)-resolution ratio, especially when employing a high-frequency resonant-raster-scanning. With a high optical resolution nature, a current mesoscopic-MPM either neglects the criterion and degrades the digital resolution to twice the pixel size, or reduces the FOV and/or the raster-scanning speed to avoid *aliasing*. We introduce a Nyquist figure-of-merit (NFOM) parameter to characterize a laser-scanning MPM in terms of its optical-resolution retrieving ability. Based on NFOM, we define the maximum aliasing-free FOV, and subsequently, a cross-over excitation wavelength, below which the FOV becomes NFOM-constrained irrespective of an optimized optical design. We validate our idea in a custom-built mesoscopic-MPM with millimeter-scale FOV yielding an ultra-high FOV-resolution ratio of >3,000, while securing up-to a 1.6 mm Nyquist-satisfied aliasing-free FOV, a ~400 nm lateral resolution, and a 70 M/s effective voxel-sampling rate, all at the same time.

INTRODUCTION

Compared to single-photon and camera-based imaging systems, with a better penetration capability due to the use of near-infrared (NIR) excitation spectrum and excitation localization of nonlinear optical absorption, a laser-scanning multiphoton microscope (MPM) becomes a promising candidate for deep intact tissue imaging while maintaining high enough three-dimensional (3D)-resolution (Denk et al., 1990; Helmchen and Denk, 2005; Theer et al., 2003; Ntziachristos, 2010; Jacques, 2013; Kobat et al., 2009; Horton et al., 2013; Horton and Xu, 2015; Rosenegger et al., 2014; Chakraborty et al., 2019). To accomplish a high-speed laser-raster-scanning of a mesoscale volumetric tissue-sample with a reduced necessity of digital-image-stitching operations, an extended FOV becomes an imperative requirement. Nevertheless, the FOV of a traditional MPM is typically limited to <1 mm^2 while preserving a submicron optical resolution. It is however important to note that with the advent of a wide variety of moderate or low magnification objective lenses with moderate numerical apertures (NAs), it is becoming feasible to extend an MPM FOV up-to several millimeters while still preserving an adequate optical resolution. Being a digital microscopy system however, an adequate digitization facility becomes another important aspect to retrieve such high optical resolution over the extended FOV under observation. That is to say, an adequate number of pixels on the digitized image is essential. While to secure the same yet maintaining a fast raster-scanning, a high enough effective voxel-sampling rate is required to satisfy or even exceed the respective Nyquist-Shannon criterion (Nyquist, 1928; Shannon, 1949), which demands *the digitized size of each sampling pixel to be at least half of the smallest resolvable spacing in order to prevent the phenomenon of aliasing, which essentially converts the optics-limited high spatial frequencies of the objects into low spatial frequencies in the final image by the Moiré effect* (Pawley, 2006; Heintzmann and Sheppard, 2007). An effective voxel-sampling rate, in this case, can be realized as an image-pixel-sampling rate, i.e., the number of pixels on the digitized image acquired in a unit second. A laser-scanning MPM typically uses a pulsed laser source for an efficient nonlinear excitation, where each digitized voxel or image-pixel is expected to correspond to at least one optical pulse. Thus, an MPM can reach a sampling rate as high as the repetition-rate of the laser while employing a pulse-synchronized digitization (Prevedel et al., 2016; Weisenburger et al., 2019).

[1]Department of Electrical Engineering and Graduate Institute of Photonics and Optoelectronics, National Taiwan University, Taipei 10617, Taiwan

[2]Department of Life Science, National Taiwan University, Taipei 10617, Taiwan

[3]Graduate Institute of Biomedical Electronics and Bioinformatics, National Taiwan University, Taipei 10617, Taiwan

[4]Molecular Imaging Center, National Taiwan University, Taipei 10617, Taiwan

[5]Lead contact

*Correspondence:: sun@ntu.edu.tw

https://doi.org/10.1016/j.isci.2021.103041

Following the same, it becomes feasible to enable a high sampling rate in an MPM simply by opting to a high-repetition-rate laser source. However, despite securing a high sampling rate, a subsequent down-scaling operation to the digitized dataset typically in an attempt to improve signal-to-noise ratio (SNR) by means of an interpolation and/or pixel-binning method might lead to *aliasing* and thus might degrade the digital resolution. As a matter of fact, in such a digital microscopy system, the effective digital resolution not only depends on the objective's NA and excitation wavelength, but also gets affected by the associated digitization and image-formation strategies. Remarkably, an ultra-high effective voxel-sampling rate becomes necessary when one simultaneously targets an extended FOV, a high digital resolution, and a fast resonant-raster-scanning. In such a scenario, overcoming the Nyquist-restriction in a laser-scanning MPM becomes challenging, as the maximum effective voxel-sampling rate is essentially limited by the laser repetition-rate. Note that an undersampling-induced *aliasing* in such a case essentially degrades the effective digital resolution of the system to twice the effective pixel size, and enforces one to reduce the raster-scanning speed and/or the imaging area to retrieve the best optical resolution.

Over the past several years, quite a few researchers have successfully addressed various design challenges to extend the FOV of a laser-scanning MPM, and demonstrated their ultra-large FOVs up-to several square millimeters (Tsai et al., 2015; Bumstead et al., 2018; Terada et al., 2018; Stirman et al., 2016; Balu et al., 2016; Sofroniew et al., 2016). Remarkably, by means of moderate- or high-NA objective lenses, the prior arts successfully preserved high enough optical resolutions over their extended-FOVs as per their experimental requirements or specific research goals. Most of such prior arts thus secured substantial improvement to the FOV-resolution ratios, as being enlisted in Table 1. In addition, several of these prior arts employed high-frequency resonant-mirrors to avail a fast-enough raster-scanning. Despite such substantial improvements being contributed to the mesoscopic-MPM modality, to the best of our knowledge, the significance of the Nyquist-Shannon sampling theorem to correlate its direct consequences over the maximum aliasing-free FOV is not yet well-explored to date. Especially for an MPM with an ultra-high FOV-resolution ratio, the issue of aliased digitization is indeed an important aspect to deal with, to unlock a large aliasing-free FOV with a submicron effective digital resolution while simultaneously preserving a fast resonant-raster-scanning.

In this paper, based on the Nyquist-Shannon sampling theorem we first formulate the minimum required repetition-rate of a pulsed laser source to fulfill the Nyquist-Shannon criterion for a given laser-scanning MPM with a specific FOV. To characterize such an MPM in terms of its reliable digitization capability, we formulate a Nyquist figure-of-merit (NFOM) parameter which indicates whether or not the system is capable of retrieving the best optical resolution. For the digitization to be aliasing-free, the value of NFOM must be greater than or at least equal to one. Taking NFOM into account, we then derive the maximum allowed FOV for a given laser repetition-rate, fast-axis scanner frequency, excitation wavelength, and objective's NA. Beyond this theoretical limit, the FOV will get aliased and the effective resolution will tend to degrade regardless of its superior optical design. For an MPM with an optimized optical FOV design, we further study the cross-over excitation wavelength, below which the FOV gets constrained by the respective NFOM and becomes wavelength dependent. Based on our derivation, we justify that in order to maximize the FOV while neither compromising the digital resolution nor the raster-scanning speed, the key solution is to enable an ultra-high voxel-sampling rate by means of a high-repetition-rate pulsed laser source, where a one-pulse-per-voxel synchronized acquisition is assumed for the optimum case. Our derivation further remarks that for a laser-scanning MPM with a high-NA objective lens but using a low-repetition-rate pulsed laser, it is not feasible to achieve a large millimeter-scale FOV without getting aliased unless the raster-scanning speed is greatly slowed down.

To validate our derivation experimentally, a design-optimized mesoscopic MPM was custom-built (Borah et al., 2020; Sun and Borah, 2019) (refer to STAR Methods) to yield an optics-limited FOV of up-to 1.6 × 1.6 mm^2 whereas preserving a submicron lateral resolution with a 0.95 NA objective lens. By implementing a regular 70 MHz femtosecond laser following our design guideline, we successfully achieved aliasing-free MPM imaging, i.e., NFOM $\geq$ 1, with an FOV-resolution ratio of more than 3,000. To validate the optical-zoom-free submicron resolution retrievability, we performed two-photon imaging of biological tissue samples with fine enough structures, and reliably retrieved them without shrinking down the 1.6 × 1.6 mm^2 imaging area if the excitation wavelength is longer than 912 nm. Our experimental study further confirms the Nyquist-Shannon sampling theorem in a laser-scanning MPM, as well as the derived cross-over excitation wavelength. By shifting the excitation wavelength down to around 919 nm which is close to this cross-over wavelength, a resolution-optimized mesoscopic MPM was also demonstrated with the

Table 1. A comparison of a few of the state-of-the-art large-FOV high-lateral-resolution MPMs

Literature	Fast-axis scanner type	Numerical aperture (NA)	Axial resolution (μm) (optical; reported)	Reported extended FOV (approx.)	Estimated pixel size (fast-axis) (μm)	Lateral resolution (μm) (optical; reported)	Lateral resolution (μm) (digital; limited by Nyquist-Shannon sampling theory)	Reported fast-axis FOV/ reported resolution	Estimated effective voxel-sampling rate (M/s)	Estimated NFOM (using reported resolution)
Tsai et al. (2015)	Galvanometric	0.28	14	8 × 10 mm^2	4	1	8	8000	<1	0.13
Bumstead et al. (2018)	Galvanometric	0.22	28	4.95 × 4.95 mm^2	4.95	1.7	9.9	2912	<1	0.17
Balu et al. (2016)	Resonant (4 kHz)	1.05	3.3	0.8 × 0.8 mm^2	0.5	0.5	1	1600	12.8	0.5
Stirman et al. (2016)	Resonant (4 kHz)	0.43	12.1	3.5 mm (width)	1.71	1.2	3.42	2917	16.4	0.35
Terada et al. (2018)	Resonant (8 kHz)	0.6	9.96	1.2 × 3.5 mm^2	2.34	1.26	4.69	952	8.2	0.27
This report	Resonant (4 kHz)	0.95	2 $_{@1070\ nm}$	1.6 × 1.6 mm^2	0.18	0.48 $_{@1070\ nm}$	0.48 $_{@1070\ nm}$	>3000 (above λ_c)	70	≥1
				1.6 × 1.6 mm^2	0.18	0.41 $_{@919\ nm}$	0.41 $_{@919\ nm}$	>3800 (near λ_c)		
				1.42 × 1.42 mm^2	0.16	0.37 $_{@824\ nm}$	0.37 $_{@824\ nm}$	>3800 (below λ_c)		

Note: The NFOMs (would be discussed in following sections) in this table were calculated considering reported optical resolutions, following, NFOM = 0.5 r_{opt}/P_s; where, r_{opt} and P_s are reported optical lateral resolution and estimated fast-axis pixel size, respectively. Parameters cited/estimated in this table are based on the reported results in each case, to the best of our knowledge.

1.6 × 1.6 mm^2 FOV, while maintaining NFOM = 1 and ~400 nm lateral resolution with a maximized FOV-resolution ratio of more than 3,800. Whereas, our study further confirmed that with an excitation shorter than this cross-over wavelength, we had to shrink down the FOV to rescue an NFOM of at least 1, i.e., the aliasing-free FOV in this regime is wavelength-dependent and is limited by Nyquist-Shannon criterion rather than the optical system design. Our study and demonstration of the mesoscopic MPM with an ultra-high FOV-resolution ratio can serve as a guideline to eliminate the final MPM barrier of aliased digitization and to enable deep-tissue volumetric MPM imaging with simultaneously an ultra-large aliasing-free FOV and a submicron digital resolution without compromising the raster-scanning speed.

RESULTS

Formulation of Nyquist figure-of-merit (NFOM)

To properly digitize the smallest optically resolvable spacing in a digital imaging system, the pixel size must be at least half of this smallest resolvable spacing, called the Nyquist-Shannon criterion (Nyquist, 1928; Shannon, 1949; Pawley, 2006; Heintzmann and Sheppard, 2007), which must be satisfied to avoid the phenomenon of aliasing. For an objective lens with a specific value of NA, its smallest resolvable lateral spacing, i.e., the lateral resolution can be estimated by the full width half maximum (FWHM) of the lateral cross section obtained by imaging a small enough structure. Theoretically, for a high-NA (>0.7) objective lens, the lateral resolution (FWHM) for multiphoton fluorescence can be described as (Zipfel et al., 2003; Sheppard and Gu, 1990)

$$r^{FWHM} = \frac{0.541\ \lambda_{exc}}{\sqrt{n}\ NA^{0.91}}, \qquad \text{(Equation 1)}$$

where λ_{exc} and n stand for excitation wavelength and order of the multiphoton process, respectively. In a pulsed-laser based point scanning MPM, fulfilling/exceeding the Nyquist-Shannon criterion for an aliasing-free maximum fast-axis field of view of FOV_{max} with a specific lateral resolution of r^{FWHM} requires the repetition-rate (R) of the pulsed laser source to be

$$R \geq V_{min}\ N, \quad \text{and} \quad V_{min} = \frac{4\ f\ FOV_{max}}{r^{FWHM}}; \qquad \text{(Equation 2)}$$

where V_{min} is the minimum voxel-sampling rate required to fulfill the Nyquist-Shannon criterion, N (≥1) is an integer signifying number of optical pulse(s) per voxel, and f is the fast-axis frequency for either a resonant or a galvanometer-based scanner. Using Equation (1), V_{min} can be redefined for an MPM with a high-NA (>0.7) objective lens as

$$V_{min} = \frac{7.3937\sqrt{n}\ NA^{0.91}\ f\ FOV_{max}}{\lambda_{exc}}. \qquad \text{(Equation 3)}$$

As V_{min} is directly proportional to f and FOV_{max}, and inversely proportional to λ_{exc}, for a given value of V_{min}, to extend the aliasing-free FOV while imaging with a high-NA objective lens, one must either decrease the fast-axis scanning frequency sacrificing the imaging speed, and/or increase the excitation wavelength sacrificing the resolution. Therefore, the only way left to neither compromise speed nor resolution is to enhance the voxel-sampling rate sufficiently. For the optimized condition, following N = 1 in Equation (2) inequality, the lowest required repetition-rate of the laser would thus be equal to the minimum voxel-sampling rate, i.e., $R_{min} = V_{min}$. Thus, for a given MPM, the required value of R_{min} can be estimated from Equation (3) based on desired FOV_{max} and choices of NA, f, and λ_{exc}. For instance, if one employs an 8 kHz fast-axis scanner and a 1.0 NA objective lens for two-photon imaging at 920 nm excitation, for achieving a 2 mm-wide fast-axis FOV, the minimum required voxel-sampling rate will be ~181.86 M/s, and hence the laser repetition-rate must be at least ~181.86 MHz. This requirement can be of course relaxed to ~90.9 MHz with a 4 kHz fast-axis scanner.

Considering Equations (2) and (3), for a straightforward assessment of the optical-resolution retrieving capability of a laser-scanning MPM, we formulate a Nyquist figure-of-merit (NFOM) parameter as follows

$$NFOM = \frac{0.1353\ R\ \lambda_{exc}}{\sqrt{n}\ N\ f\ NA^{0.91}\ FOV_{max}}. \qquad \text{(Equation 4)}$$

Formulation of maximum achievable aliasing-free field of view (FOV_{max}) and cross-over excitation wavelength

For the digitization to be aliasing-free, NFOM must be greater than or at least equal to 1. For a given λ_{exc}, an attempt to enhance the FOV_{max} with a high- f and/or a high-NA configuration will tend to degrade the

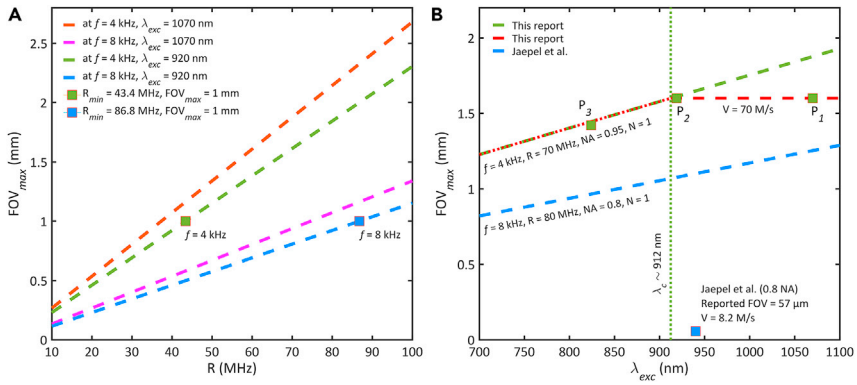

Figure 1. Plots of FOV_{max} for a laser-scanning MPM

(A) FOV_{max} with respect to R at NA = 0.95 & N = 1. For FOV_{max} = 1 mm, the green & blue colored solid squares correspond to R = 43.4 MHz at f = 4 kHz & R = 86.8 MHz at f = 8 kHz, respectively.

(B) FOV_{max} with respect to λ_{exc}, where the green-dashed line represents FOV_{max} of this report at NA = 0.95, N = 1, and f = 4 kHz; green-dotted line marks the cross-over excitation wavelength, i.e., λ_c = 912 nm; red-dashed and red-dotted lines depict the optics-limited and NFOM-constrained FOVs, respectively. P_1, P_2, and P_3 are three imaging conditions each with 70 M/s effective voxel-sampling rate, at excitation wavelengths of 1,070 nm ($>\lambda_c$) with NFOM>1 for 1.6 mm-wide optics-limited FOV, at 919 nm ($\sim \lambda_c$) with NFOM = 1 for the same 1.6 mm-wide but resolution-optimized FOV, and at 824 nm ($<\lambda_c$) with NFOM = 1 for an NFOM-constrained 1.42 mm-wide FOV, respectively. Blue-dashed line represents theoretical FOV_{max} limitation for the experimental condition of a prior report by Jaepel et al. (2017) with an 80 MHz pulsed laser. The blue solid square marks the previous experimental FOV (Jaepel et al., 2017), which is much lower than the theoretical limitation derived in this paper.

NFOM to be less than 1, which must be rescued by means of a high-R laser. Incorporating an even higher-NA objective lens, and/or even lower λ_{exc} will demand an even higher value of R to maintain a specific FOV_{max}. For instance, a ~1.4 times higher value of R will be required when NA is enhanced from 1.0 to 1.45; likewise, lowering λ_{exc} from 1,070 nm to 760 nm, will require a ~1.4 times higher R, the remaining parameters kept unchanged in each case.

For the optimized case with NFOM = 1 and N = 1, the aliasing-free FOV_{max} for a specified set of laser, fast-axis scanner, and objective lens can be thus estimated as

$$FOV_{max} = \frac{0.1353 \quad R \quad \lambda_{exc}}{\sqrt{n} \quad f \; NA^{0.91}}. \qquad \text{(Equation 5)}$$

Figure 1A plots the maximum aliasing-free field of view, FOV_{max} from Equation (5) as a function of R for the fixed values of NA = 0.95 and N = 1. As depicted by the data points, to achieve an aliasing-free FOV_{max} of 1 mm to be operated up-to a minimum λ_{exc} of 920 nm, the laser repetition-rate must be at least 43.4 MHz for a 4 kHz scanner, and at least 86.8 MHz for an 8 kHz scanner. This essentially justifies that for a high-NA objective lens employed with a high-frequency fast-axis scanner, the only way to extend the aliasing-free FOV_{max} beyond ~1 mm is to opt for a pulsed laser source with high enough repetition-rate (R) to enable an ultra-high effective voxel-sampling rate (V).

Based on Equation (5), Figure 1B plots the FOV_{max} as a function of λ_{exc} for two high-NA MPM settings each with NFOM ≥ 1, where the blue-dashed line corresponds to the experimental parameters of a prior report by Jaepel et al. (2017). In this case, although an 80 MHz pulsed laser was employed for excitation, the previously reported aliasing-free FOV is ~19 times lower than our idealized theoretical value FOV_{max} with N = 1 (blue-dashed line). Part of the discrepancy can be attributed to the low effective voxel-sampling rate of 8.2 M/s. On the other hand, our report studied the case of a femtosecond laser with a 70 MHz repetition-rate, which is on the same order or slightly lower than most commercial femtosecond lasers. As shown in the green-dashed line, which represents FOV_{max} with NA = 0.95, N = 1, and f = 4 kHz, with a maximized effective voxel-sampling rate of 70 M/s, this report predicts the possibility to achieve an aliasing-free FOV_{max} much greater than 1 mm across the excitation wavelengths between 700 and 1,100 nm while digitally preserving the diffraction-limited nonlinear optical resolution. Our calculation also justifies the impact of true/effective voxel-sampling rate (V) and hence the laser repetition-rate (R) for a large-FOV aliasing-free imaging.

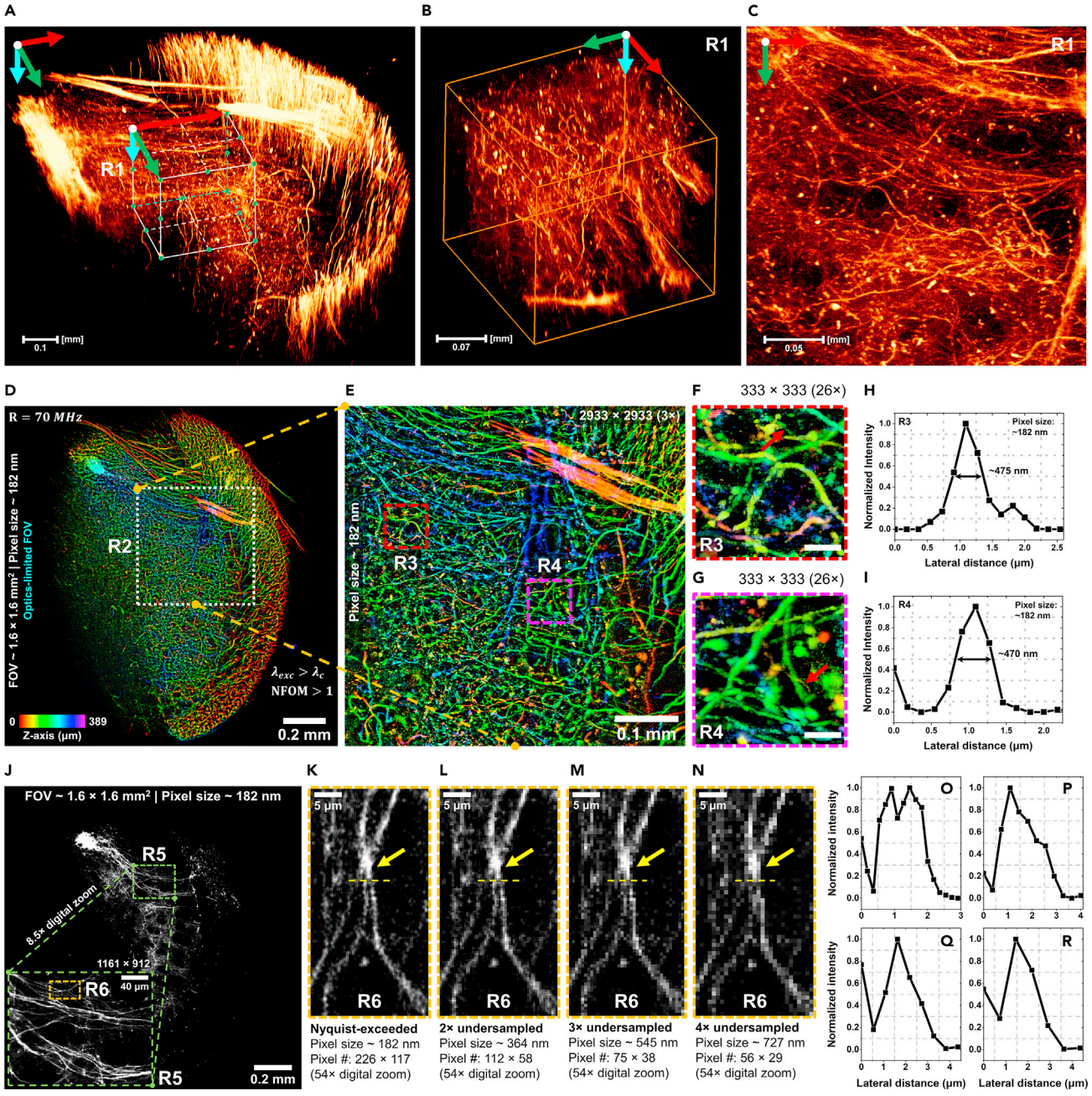

Figure 2. Demonstration of stitch-free large-FOV two-photon imaging with Nyquist-exceeded sampling

A coronal section from medulla of a Nav1.8-tdTomato mouse was scanned across 1.6 × 1.6 × 0.4 mm^3 volume with a voxel size of 0.182 × 0.182 × 0.3 μm^3.

(A) 3D-rendered volume (using Amira) in inclined view.

(B) Enlarged 3D cropped ROI R1 marked in *A*, providing lateral & axial views.

(C) Top view of the ROI R1. Red, green & cyan colored axes represent X, Y & Z axes, respectively. Scale bars for *A*-*C*: 0.1 mm, 0.07 mm, and 0.05 mm, respectively.

(D) 2D representation of the acquired volume with Z-projection (color coded Z axis), scale bar = 0.2 mm.

(E) 3× digitally zoomed ROI R2 (marked in *D*), scale bar = 0.1 mm, showing color-coded fine fibers.

(F and G) 26× digitally zoomed ROIs R3 & R4 in *E*; red arrows mark submicron structures, scale bar = 15 μm.

(H and I) Intensity profiles across the fine fibers marked in *F* & *G*, respectively; revealing FWHMs of 475 nm for *H*, and 470 nm for *I*.

(J) A Z-projected 9 μm-thick section from the same acquired data, scale bar = 0.2 mm.

Figure 2. *Continued*

(K–N) Enlarged vertically oriented views of the ROI R6 marked inside ROI R5 in *J*, obtained with (K) Nyquist-exceeded (pixel size: 182 nm), (L) 2× undersampled (pixel size: 364 nm),

(M) 3× undersampled (pixel size: 545 nm), and (N) 4× undersampled (pixel size: 727 nm) cases, respectively (scale bar = 5 μm), with pixel numbers of 226 × 117, 112 × 58, 75 × 38, and 56 × 29, respectively.

(O–R) Intensity profiles along the yellow-dashed lines in *K-N*, respectively.

(O) Resolves the separation between two adjacent submicron fibers. (P-R) Essentially detect the two adjacent fibers resolved in *O* as a single fiber.

For a conventional laser-scanning system (Chun et al., 2013) with an optics-limited field of view of FOV_{OL} (Equation (S11)), we can redefine the minimum effective voxel-sampling rate, and hence the minimum laser repetition-rate required for a given laser-scanning MPM to be aliasing-free. Following Equations (3) and (S11), and considering $FOV_{max} = FOV_{OL}$, we obtain

$$V_{min} = R_{min} = \frac{14.7874\sqrt{n}\ NA^{0.91}\ f \tan|\theta_{\pm}|\ f_o\ f_s}{\lambda_{exc}\ f_t}, \qquad \text{(Equation 6)}$$

where, $\theta_{\pm}$ is the fast-axis scan-angle by the scanning mirror with respect to the optical axis, f_o, f_s, and f_t are the effective focal lengths (EFLs) of the objective lens, scan lens, and tube lens, respectively.

From Equation (5), for a laser-scanning MPM with $FOV_{OL} \leq FOV_{max}$, a cross-over excitation wavelength λ_c can be further estimated as follows. When λ_{exc} is longer than λ_c, the FOV of the system remains limited by the relevant optics. However, as λ_{exc} becomes shorter than λ_c, the FOV is rather constrained by the NFOM of the respective system. For an optics-limited resolution-optimized FOV, $\lambda_{exc} \sim \lambda_c$ is expected with

$$\lambda_c = \frac{7.3937\sqrt{n}\ f\ NA^{0.91}\ FOV_{OL}}{R}. \qquad \text{(Equation 7)}$$

Experimental demonstration and validation of the proposed theory and hypothesis

To validate our theory and hypothesis, we constructed a mesoscopic MPM utilizing off-the-shelf optomechanical components. Following Equation (6), we chose f_o, f_s, and f_t of 9 mm, 110 mm, and 166.7 mm, so that $\theta_{\pm} \sim \pm 7.7^0$ can provide up-to an FOV_{OL} of ~1.6 mm. Combining a high (0.95) NA objective lens with 9 mm EFL preserved not only a high spatial resolution, but also resulted in a large FOV-resolution ratio greater than 3,000. For two-photon imaging we further chose $\lambda_{exc} = 1070$ nm and $f = 4$ kHz, thus obtaining $V_{min} = R_{min} = 59.7$ MHz, which is lower than most of the commercially available femtosecond oscillators and is easily achievable. For demonstration, a femtosecond laser source with R = 70 MHz and $\lambda_{exc} \approx$ 1070 nm was first chosen. Following Equation (2), the value of N, being an integer, is not allowed to be more than 1 in this case, enforcing a one-pulse-per-voxel acquisition. Therefore, following Equation (5), we obtain $FOV_{max} = 1.87$ mm (>FOV_{OL}) for N = 1 case. From Equation (4), NFOM = 1.17>1; thus, the optics-limited FOV is guaranteed to be aliasing-free. In this case, from Equation (7), the cross-over excitation wavelength, λ_c was estimated to be around 912 nm.

To experimentally validate the fulfillment of the Nyquist-Shannon criterion, we performed two-photon imaging of a coronal section from the medulla of a Nav1.8-tdTomato mouse across a volume size of ~1.6 × 1.6 × 0.4 mm^3 preserving a voxel size of 0.182 × 0.182 × 0.3 μm^3. With $\lambda_{exc} \approx 1070$ nm> λ_c, the FOV was optics-limited in this case. Figure 2A depicts the stitch-free 3D-rendered volume (using Amira software, Mercury Computer Systems, USA) in an inclined view. The 3D region of interest (ROI) R1 is cropped and enlarged in Figure 2B, and its top view is presented in Figure 2C. Red, green, and cyan colored axes represent X, Y, and Z axes, respectively. Figure 2D shows a two-dimensional (2D) representation of the acquired volume with color-coded depth information, processed using ImageJ software (National Institutes of Health, USA) and OpenCV (an open-source computer vision library). No stitching/mosaicking was applied. Figure 2E shows a 3× digitally enlarged ROI R2 with 2,933 × 2,933 pixels maintaining a ~182 nm pixel size, presenting the color-coded fine fibers. With a 26× digital zoom to the original image, the ROIs R3 and R4 marked in Figure 2E are enlarged in Figures 2F and 2G, respectively, each with a pixel number of 333 × 333, with 182 nm pixel size. The red arrows in Figures 2F and 2G mark two submicron fibers. Figures 2H and 2I respectively show the intensity profiles across the fibers in Figures 2F and 2G, with FWHMs of around 475 nm and 470 nm, respectively. Figure 2J depicts a Z-projected ~9 μm-thick section from the same acquired data with pixel size of 182 nm. An 8.5× digital zoom was performed to the ROI R5 (1,161 × 912 pixels) and its enlarged view is shown in the same Figure 2J. Another ROI R6 with two adjacent submicron fibers is selected within ROI R5, with a 54× digital zoom to the original image. Figures 2K–2N respectively depict

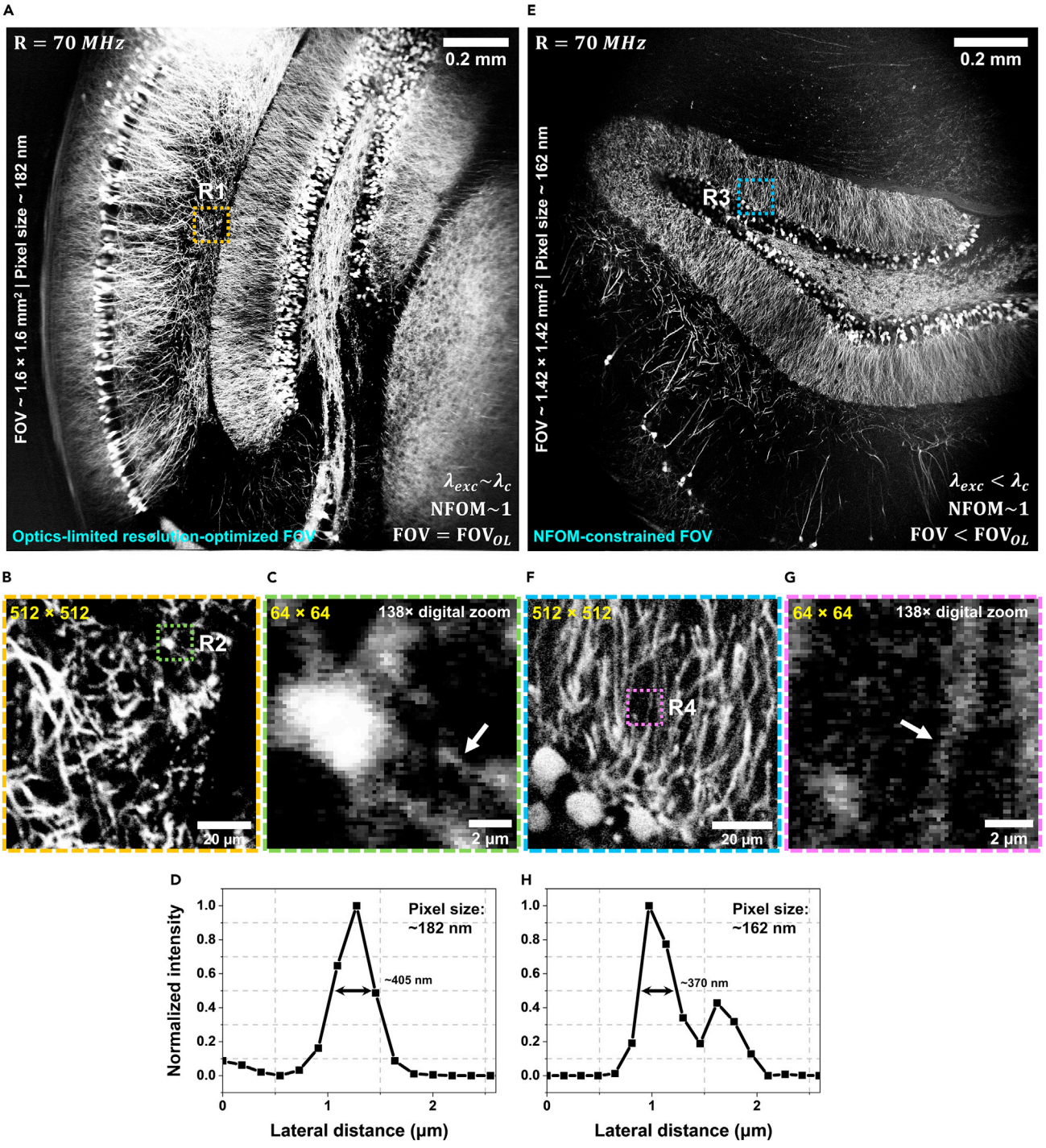

Figure 3. Two-photon imaging near & below the cross-over excitation wavelength to demonstrate an optics-limited resolution-optimized FOV & an NFOM-constrained FOV, respectively

(A) Optics-limited 1.6 mm-wide FOV at λ_{exc} = 919 nm $\sim$ λ_c & NFOM = 1; Z-projected view of 8 imaging slices at Z-step = 0.8 µm, pixel size = 182 nm, scale bar = 0.2 mm; sample: a hippocampal sagittal section from a thy1-GFP mouse.

(B and C) Enlarged ROIs R1 (512 × 512 pixels) in *A* & R2 (64 × 64 pixels) in *B*, respectively.

(D) Intensity profile across the fiber marked by the white arrow in *C* with an FWHM of 405 nm. (A–D) Justifies the best resolution for the optics-limited FOV with an FOV-resolution ratio of more than 3,800 at the optimized condition with NFOM = 1 & $\lambda_{exc} \sim \lambda_c$.

(E) NFOM-constrained 1.42 mm-wide FOV at λ_{exc} = 824 nm< λ_c; Z-projected view of 8 imaging slices at Z-step = 0.8 µm, pixel size = 162 nm, scale bar = 0.2 mm; sample: a hippocampal coronal section from an Alexa Fluor 546 (anti-GFP immunohistochemistry labeling) mouse.

Figure 3. *Continued*

(F and G) Enlarged ROIs R3 in *E* with 512 × 512 pixels & R4 in *F* with 64 × 64 pixels, respectively.

(H) Intensity profile across the white-arrow-marked fiber in *G* revealing an FWHM of 370 nm comparable to the respective r^{FWHM} of 330 nm. Scale bars in *B* & *F* are 20 μm, and *C* & *G* are 2 μm. Note: ROIs R2 & R4 in *C* & *G*, respectively, were obtained by performing 138× digital zoom to the corresponding full-FOV images.

the enlarged views of the ROI R6 with (K) Nyquist-exceeded (pixel size = 182 nm), (L) 2× undersampled (pixel size 364 nm), (M) 3× undersampled (pixel size 545 nm), and (N) 4× undersampled (pixel size 727 nm) cases (scale bar = 5 μm), with pixel numbers of 226 × 117, 112 × 58, 75 × 38, and 56 × 29, respectively. ROI R6 in *J* is vertically oriented in *K-N*. Figure 2O plots the intensity profile along the yellow-dashed line marked in Figure 2K for the Nyquist-exceeded condition, and resolves the separation between the two adjacent submicron fibers which are ~550 nm apart. On the contrary, similarly plotted intensity profiles in Figures 2P–2R, for the undersampled cases, essentially detect these two adjacent fibers as a single fiber, as the increased pixel size does not meet the Nyquist-Shannon criterion.

In Figure 1B, the green-dashed line corresponds to the FOV_{max} of our custom-built MPM plotted with respect to the excitation wavelength. For the 70 MHz laser, the cross-over excitation wavelength λ_c in our case is around 912 nm as represented by the green-dotted line in Figure 1B. In Figure 2 with an NFOM>1, we have demonstrated the Nyquist-exceeded imaging capability of the system at λ_{exc} of around 1,070 nm as indicated by point-P_1 in Figure 1B. At this condition with $\lambda_{exc} > \lambda_c$, the 1.6 mm-wide FOV was limited by optics and was lower than the FOV_{max} limit. The red-dashed line in Figure 1B represents our optics-limited FOV.

To realize not just the optics-limited but also the resolution-optimized FOV, the excitation wavelength was lowered to around 919 nm (point-P_2 in Figure 1B) approaching the cross-over wavelength (λ_c) of 912 nm. We performed two-photon imaging of a sagittal section from the hippocampus of a thy1-GFP mouse. The Z-projected view of 8 imaging slices at 0.8 μm Z-step is depicted in Figure 3A with a scale bar of 0.2 mm. An NFOM = 1 for the optics-limited 1.6 mm-wide FOV was maintained with the same pixel size of 182 nm. To investigate the high-resolution resolvability, we first mark an ROI R1 in Figure 3A with 512 × 512 pixels which is enlarged in Figure 3B with a scale bar of 20 μm. Another ROI R2 with 64 × 64 pixels is again marked inside ROI R1 in Figure 3B. Figure 3C shows the enlarged view of R2 with a scale bar of 2 μm which resolves fine submicron structures by means of the 138× digital zoom to the original image. An intensity profile obtained across the fiber marked by the white arrow in Figure 3C is plotted in Figure 3D with an FWHM of 405 nm. Thereby, an FOV-resolution ratio of more than 3,800 was enabled, not to mention without optical zooming.

To demonstrate the predicted effect of NFOM-constrained FOV as depicted by the red-dotted line in Figure 1B, we again reduced the excitation wavelength to around 824 nm which is lower than λ_c. At this condition, the aliasing-free FOV is no longer limited by the optical performance, rather it becomes NFOM-constrained which in our case is around 1.45 mm. Remarkably, such NFOM-constrained reduction to the FOV is going to be more severe for an application requiring even shorter excitation wavelength. To demonstrate this scenario, we acquired two-photon images from a coronal section of an Alexa Fluor 546 stained (anti-GFP immunohistochemistry labeling) mouse hippocampal region at λ_{exc} of around 824 nm as represented by point-P_3 in Figure 1B. Figure 3E with a scale bar of 0.2 mm depicts the Z-projected view of 8 imaging slices at 0.8 μm Z-step. Respecting the NFOM-constrain, the FOV was set to 1.42 mm with a reduced pixel size of 162 nm. The 512 × 512-pixeled ROI R3 in Figure 3E is enlarged in Figure 3F (scale bar = 20 μm) where another 64 × 64-pixeled ROI R4 is again marked. Figure 3G depicts the enlarged view of the ROI R4 with a 138× digital zoom to the full-FOV image. Figure 3H plots the intensity profile across the white-arrow-marked fine fiber in Figure 3G, revealing an FWHM of around 370 nm which is comparable to the theoretical r^{FWHM} of 330 nm.

Notably, both [$\lambda_{exc} \sim \lambda_c$]-case with optics-limited resolution-optimized FOV and [$\lambda_{exc} < \lambda_c$]-case with NFOM-constrained FOV preserved an NFOM~1, and thus 2 pixels per theoretical point spread function were ensured in each case. ImageJ and OpenCV were used for the analysis presented in Figure 3.

Feasibility of high-frame-rate MPM imaging at maximized fast-axis FOV

For a fixed fast-axis scanner which in our case is with a resonant frequency of 4 kHz, the frame rate is not affected by any change to the fast-axis scanning angle, and hence the fast-axis FOV. However, for a large

Table 2. Acquisition capability of the developed data acquisition system

Single-frame pixel number (in X and Y axes) with 4 kHz resonant scanner								
Fast X axis								
Sampling rate in mega samples per second (MSps)								
20 MSps	50 MSps	70 MSps	100 MSps	125 MSps	Slow Y axis	Largest pixel number (× 4 channels)	Maximum data size per frame (in megabytes)	Approximate frame rate (in frames per second)
2400	6224	8800	12,520	15,720	16,000	15,720 × 16,000×4	1918.9	0.49
2400	6224	8800	12,520	15,720	12,000	15,720 × 12,000×4	1439.2	0.64
2400	6224	8800	12,520	15,720	8000	15,720 × 8,000×4	959.47	0.96
2400	6224	8800	12,520	15,720	4000	15,720 × 4000×4	479.74	1.88
2400	6224	8800	12,520	15,720	1000	15,720 × 1000×4	119.93	7.87
2400	6224	8800	12,520	15,720	500	15,720 × 500×4	59.967	15.75
2400	6224	8800	12,520	15,720	250	15,720 × 250×4	29.984	31.5
2400	6224	8800	12,520	15,720	16	15,720 × 16×4	1.919	490
2400	6224	8800	12,520	15,720	8	15,720 × 8×4	0.959	980

FOV in the direction governed by the slow-axis, enough number of lines must be scanned to maintain the aliasing-free nature. For a 1 × 1 mm^2 FOV at 1,070 nm excitation wavelength and 0.95 NA, to maintain an NFOM of 1 or more, we would require at least 4663 × 4663 pixels. To acquire 4663 lines along the slow axis, the time required for a 4 kHz resonant scanner would be at least 0.58 s. Table 2 illustrates our acquisition capability at various sampling rates in terms of pixel numbers, data sizes, and frame rates. Note that our NFOM derivations are exclusively related to the fast-axis FOV. A simple way to double our frame rates is to replace the 4 kHz scanner with a standard 8 kHz one, which will however require a minimum laser repetition-rate of 119.4 MHz for a 1,070 nm excitation (Equation (3) and (6)) while maintaining an NFOM of at least 1.

It is important to note that the maximized square-shaped FOV of our system might not be suitable for those imaging applications which involve high-frame-rate functional analysis. For such requirements, the slow-axis pixel number, and hence the slow-axis FOV can be easily reduced to boost the frame rate. That is to say, the square-shaped FOV can be made rectangular in shape to enhance the frame-rate while maintaining the same fast-axis FOV. Let us consider an example here. We have a 70 M/s effective voxel-sampling rate providing a 182 nm pixel size along the fast-axis with a pixel number of 8,800. Suppose we need to perform a functional imaging at a frame rate of >30 frames per second (fps). For the same, according to our Table 2, we need to maintain 250 pixels along the slow-axis (i.e., a 46 μm slow-axis FOV). However, note that our fast-axis-maximization idea does not have any dependency with this slow axis pixel number. That is to say, by following our idea, the FOV can be maximized to 1,600 × 46 μm^2 (8,800 × 250 pixels), remarkably while maintaining the same >30 fps frame rate. Thus, our idea can bring a significant improvement to the acquisition capability of such a high-frame-rate MPM to maximize the fast-axis FOV and thereby the FOV-resolution ratio, while neither sacrificing the resolution nor the targeted frame-rate.

Assessment of image quality in terms of signal-to-noise ratio (SNR), signal-to-background ratio (SBR), and contrast ratio under different frame-accumulation conditions

An undersampled acquisition results in a lower SNR (Virtue and Lustig, 2017) owing to fewer acquired data in each frame. As a consequence, multiple frame accumulation/averaging is required to achieve a high-SNR image which indeed limits the practical imaging speed of the system. To maintain a faster imaging speed, a sufficient SNR for a single-frame-image is quite helpful to avoid prolonged accumulation.

To assess the image quality in terms of SNR, SBR, and contrast ratio, a piece of sciatic nerve of the Nav1.8-tdTomato mouse was imaged over the extended FOV maintaining a pixel size of ~182 nm at an excitation wavelength of around 1,070 nm. The sample was excited with an average laser power of ~45 mW and the supply voltage to the PMT was set at −600 V. Figures 4A–4D depict cropped two-photon images each with 2,200 × 2,100 pixels (scale bar of 0.1 mm), obtained under frame averaging of (A) none (single frame), (B) 3, (C) 5, and (D) 7, respectively. For each cropped image, we select a 45 × 45-sized ROI from a signal location and another 45 × 45-sized ROI from a noisy-background location, being marked by the yellow- and red-

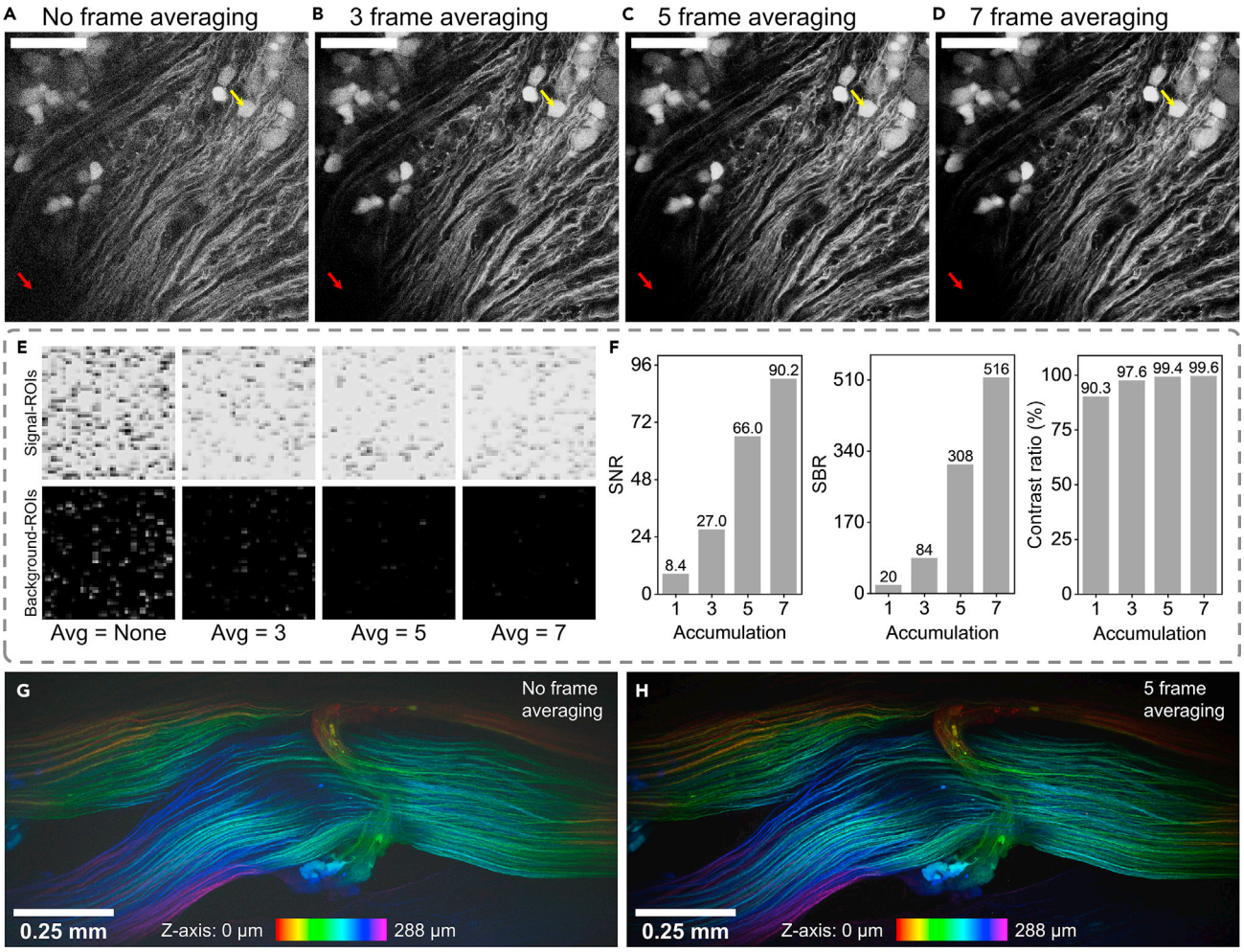

Figure 4. Image quality assessment in terms of signal-to-noise ratio (SNR), signal-to-background ratio (SBR), and contrast ratio under different frame-accumulation conditions

(A–D) Two-photon images (scale bars = 0.1 mm), each with pixel size of ~182 nm, obtained under frame averaging of (A) none (single frame), (B) 3, (C) 5, and (D) 7, respectively. Sample: a piece of sciatic nerve of a Nav1.8-tdTomato mouse.

(E) Enlarged 45 × 45-sized signal- and background-ROIs taken from the yellow- and red-arrow marked locations in each case of *A-D*.

(F) Plots SNR, SBR, and contrast ratio evaluated using the signal- and background-ROIs in *E*, which are respectively found as (A) 8.4, 20, 90.3%, (B) 27.0, 84, 97.6%, (C) 66.0, 308, 99.4%, and (D) 90.2, 516, 99.6%. A frame averaging of 3 was sufficient to attain an SNR of >20, an SBR of >80, and a contrast ratio of >97%.

(G and H) Maximal-intensity Z-projections (scale bar = 0.25 mm) of two stacks (scanned within a fixed location of the same sample) acquired under frame averaging of (G) none, and (H) 5, respectively. ImageJ was used for the analysis.

arrows, respectively. Figure 4E depicts the enlarged views of these signal- and background-ROIs sequentially for each case. For each signal-ROI, we evaluate the mean (μ_1), and for each background-ROI, we evaluate the mean (μ_2) and standard deviation (σ). For each case, SNR, SBR, and contrast ratio are plotted in Figure 4F, which are defined and evaluated as μ_1/σ, μ_1/μ_2, and $((\mu_1 - \mu_2)/(\mu_1 + \mu_2)) \times 100\%$, respectively. For Figures 4A–4D, SNRs are respectively found to be 8.4, 27.0, 66.0, and 90.2; SBRs are respectively found to be 20, 84, 308, and 516; and contrast ratios are respectively found as 90.3%, 97.6%, 99.4%, and 99.6%. It is thus observed that a frame averaging of 3 is sufficient to attain an SNR of >20, an SBR of >80, and a contrast ratio of >97%. In this situation, the imaging speed is reduced to ~0.3 fps with the 4 kHz resonant scanning system (refer to Table 2 for detailed frame-rate information).

To show the feasibility of single frame (no accumulation/averaging) acquisition, we imaged a fixed location of the same sample acquiring two stacks (360 slices at 0.8 µm Z-steps) under frame averaging of none (single frame) at 0.87 fps, and 5 at 0.17 fps, respectively, and their maximal-intensity Z-projections are shown in

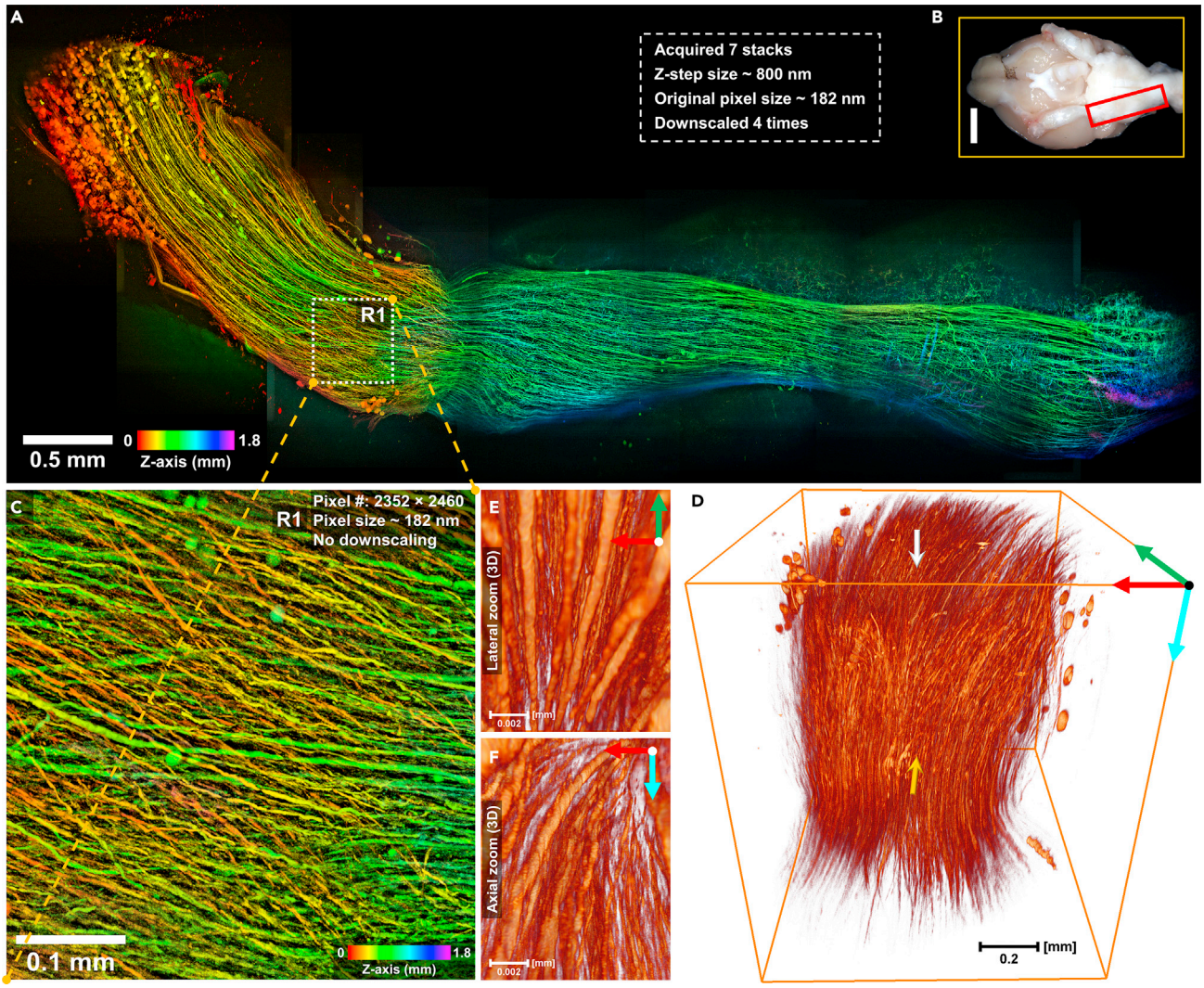

Figure 5. Demonstration of a mesoscale volumetric imaging

(A and B) 2D-representation of an intact trigeminal tract (scale bar = 0.5 mm) acquired from a Nav1.8-tdTomato mouse whole-brain (clarified) sample (scanned within the red rectangular ROI marked on the intact brain (before clarifying) as shown in *B* with a scale bar of 3 mm), where maximal-intensity-projected 7 imaging stacks were manually stitched together to form the complete view.

(C) A cropped and enlarged region, scale bar = 0.1 mm, pixel number = 2,352 × 2,460, corresponding to the ROI R1 marked in *A*.

(D) 3D-rendering of a stack (acquired near R1 in *A*) using Amira, representing an inclined view of the volume, scale bar = 0.2 mm.

(E and F) Lateral & axial views of fine fibers, respectively, scale bar = 0.002 mm. Virtual camera was moved inside the stack through top (XY) & side (XZ) planes along the white & yellow arrowed directions in *D*, respectively. The red, green & cyan colored axes represent X, Y & Z axes, respectively.

Figures 4G and 4H, respectively (scale bar = 0.25 mm). The slices were color coded for visualization of the depth information.

Mesoscale 3D imaging of an ultra-large volumetric tissue-sample

To demonstrate our high-resolution mesoscale 3D imaging capability with the ultra-high effective voxel-sampling rate, we performed two-photon imaging of an intact trigeminal tract (Westberg and Kolta, 2011) from a Nav1.8-tdTomato mouse whole-brain (clarified) sample, acquiring 7 imaging stacks with a total of 9,112 slices at a voxel size of ~0.182 × 0.182 × 0.8 μm^3. Owing to system memory limitation, for stitching and 3D-rendering purposes, we applied 4× downscaling to the acquired data. We performed maximal intensity projection of each stack and manually stitched them to form the complete view as depicted in Figure 5A. ImageJ and OpenCV were used for processing. The trigeminal tract traveled longitudinally and

formed dense network mainly with the trigeminal principal sensory nucleus (at the rostral part) and spinal trigeminal complex (at the caudal part). The imaging location is marked by the red rectangular ROI on the intact brain (before clarifying) as shown in Figure 5B with a scale bar of 3 mm. Figure 5C represents an enlarged region with original pixel number of 2,352 × 2,460 corresponding to the ROI R1 marked in Figure 5A, where the fine color-coded fibers can be traced. We further performed a 3D-rendering of a stack acquired near ROI R1 using Amira. Figure 5D represents an inclined view of the stack. We moved the virtual camera through top (XY) and side (XZ) planes along the white and yellow arrowed directions in Figure 5D, respectively, and the virtual camera views of the fine fibers in both cases are depicted in Figures 5E and 5F, respectively, with scale bar modified from 0.2 mm to 0.002 mm by means of digital zooming. The red, green, and cyan colored axes in Figures 5D–5F represent X, Y, and Z axes, respectively.

DISCUSSION

The purpose of an extended FOV while simultaneously preserving a high spatial resolution is to enable one to resolve fine submicron structures throughout the FOV without optical zooming, and thereby to facilitate a faster imaging speed with minimal digital image stitching. However, for an MPM with an ultra-high FOV-resolution ratio together with a high enough raster-scanning speed, fulfillment of the Nyquist-Shannon criterion becomes challenging because of requirement of an ultra-high effective voxel-sampling rate. A comparison of a few of the state-of-the-art large-FOV high-lateral-resolution MPMs (Tsai et al., 2015; Bumstead et al., 2018; Terada et al., 2018; Stirman et al., 2016; Balu et al., 2016) in terms of FOV-resolution-ratios and NFOMs is enlisted in Table 1. Remarkably, each prior report with an inadequate effective voxel-sampling rate encountered an NFOM<1, and thus a degraded effective resolution in each case. Sofroniew et al. (2016) demonstrated a 5 mm-wide FOV by means of combining multiple 600 μm-wide strips, however, was limited by pixel size to meet the Nyquist-Shannon criterion for the 0.66 μm reported resolution. Tsai et al. (2015) reported an ultra-high FOV-resolution ratio of 8,000 preserving a 1 μm lateral resolution by means of a low ($\leq$0.3) NA objective lens, however encountered a poor NFOM of 0.125. A lower value of NA typically leads to a poor axial resolution. Besides, a poor NFOM induces substantial degradation to the effective lateral resolution as well. Therefore, a low-NA poor-NFOM system results in a severely poor effective 3D resolution.

To achieve NFOM$\geq$1 for our custom built MPM, the minimum required effective voxel-sampling rate was estimated to be 59.7 MHz (Equation (3) or (6)). Therefore, with a 70 MHz pulsed laser, Equation (2) restricts us to follow N = 1, i.e., a one-pulse-per-voxel synchronized acquisition to meet the requirement of voxel-sampling rate. Despite being a promising idea, to date, this has not been implicated in a laser-scanning MPM aiming to maximize the effective voxel-sampling rate so as to fulfil/exceed the Nyquist-Shannon criterion for a large FOV-resolution ratio. It is remarkable that the prior literatures related to pulse-level synchronized-sampling often targeted small-FOV MPMs, and either employed a low-repetition-rate pulsed laser source, or lowered down the effective voxel-sampling rate (Prevedel et al., 2016; Weisenburger et al., 2019, Kong et al., 2015; Gil et al., 2018; Li et al., 2020; Xiao and Mertz, 2019), mostly to improve the SNR. A low-repetition-rate laser is usually employed when aiming for a high pulse energy to secure a high SNR. Furthermore, whether the sampling being pulse-synchronized or not, a reduction to the effective voxel-sampling rate by means of any interpolation and/or pixel-binning method essentially degrades the NFOM irrespective of a high-SNR and might induce irreversible resolution loss. On the other hand, our idea contradicts both the prior trends, i.e., usage of a low-repetition-rate laser source and/or reduction of the effective voxel-sampling rate especially when a non-aliased extended FOV is a concern. Our idea of maximizing the aliasing-free FOV enforces a maximized effective voxel-sampling rate limited by the repetition-rate of a high pulse-rate laser at N = 1 for the acceptable condition.

For a conventional MPM with N = 1, because of lower pixel dwell time, a reduced photon budget, and hence a poor SNR can be a cause of concern. However, for a mesoscopic MPM with a large FOV, this situation is different. With N = 1, the reduced photon budget can be compensated by a higher excitation power without damaging the sample; since, the average power is now covering much extended area, and thus the power density over a unit area will decrease and will allow higher average power after the objective lens. For instance, by extending the FOV from 0.4 × 0.4 mm^2 to 1.6 × 1.6 mm^2, 16 times average output power will be needed to maintain the same optical power density over the unit area. For N = 1, there will be only two consecutive pulses to be focused inside the point spread function, and thus even with a time interval of the order of the fluorescence lifetime, the risk of bleaching is minimized. Our study thus yields a conclusion that for an ideal system with NFOM = 1 and N = 1, a high enough repetition-rate-laser

with reasonably increased excitation power will allow the photon budget issue to be improved without much compromising the imaging speed. We utilized an average power of $\leq$45 mW for the experiments presented in this paper. In addition to the excitation power, collection of at least 8 voxels per focal volume for a Nyquist-exceeded volumetric imaging further improves the SNR. With no frame accumulation, an SNR over 8 was achieved, which was further improved to over 20 with a frame accumulation of 3.

We stated the repetition-rate (R) of the pulsed laser source to be the only enhanceable parameter for achieving NFOM$\geq$1 while not compromising with the raster-scanning speed and/or the effective resolution. For a low-repetition-rate pulsed laser, one must reduce the fast-axis scanner frequency significantly to make NFOM$\geq$1. For instance, following Equation (5) for a two-photon process with R = 1 MHz, λ_{exc} = 1070 nm, NA = 0.95, and FOV_{max} = 1.6 mm, to achieve NFOM = 1, the maximum allowed fast-axis frequency (f) is 67 Hz only, taking 7.46 ms per fast-axis line. Hence, for a square-shaped FOV of 1.6 × 1.6 mm^2, a total of 55.64 s per frame will be required to fulfill the Nyquist-Shannon criterion with a pixel number of 7,459 × 7,459 for an r^{FWHM} of 429 nm, leading to a severely poor imaging speed of 0.018 fps. Hence, to maintain a large-field high-resolution imaging at high-speed with a resonant fast-axis scanner, and to simultaneously maintain NFOM$\geq$1, a high-repetition-rate pulsed laser is the only key. The imaging speed can be further enhanced by employing an even faster fast-axis scanner which will however demand an even higher repetition-rate pulsed laser to maintain NFOM$\geq$1. The relevant fluorescence lifetime should be considered while choosing an appropriate repetition-rate (Charan et al., 2018). Most of the fluorescent dyes have a fluorescence lifetime of 1–5 ns, and therefore the pixel dwell time for point scanning needs to be >5 ns, and hence the value of R prefers not to be much higher than 200 MHz.

Even though we are not able to build a system capable of providing an aberration-free and vignetting-free extended-FOV with a full-field diffraction-limited performance, our validation of the Nyquist-exceeding capability in the central area of the FOV is a proof of the Nyquist-exceeding capability across the entire FOV, because the actual digital pixel size at the edge area is the same or even smaller than that in the central area owing to the slower scanner speed and the spatial resolution at the edge is either the same (for a future ideal system) or poorer than that in the central imaging area.

With our demonstrated mesoscope, no optical zooming was employed to obtain the high-magnification images presented in this study. Instead, all submicron structures were retrieved by digitally zooming into the respective full-FOV images. Each pixel size we specified was identical in both horizontal and vertical directions. Hence, the Nyquist-Shannon criterion was satisfied in both X and Y axes identically. Note that we used the theoretical resolution of the system in Equation (1) to evaluate our NFOM, ensuring retrievability of the best possible lateral resolution. This basically guarantees that digitization of all regions of the extended FOV fulfills the Nyquist-Shannon criterion. Additionally, whether we image at a superficial plane where the optical resolution is usually higher or close enough to the theoretical limit, or at a deeper plane where the optical resolution might tend to be lower, it is always guaranteed that the Nyquist-Shannon criterion is satisfied.

In the axial direction, a step-size of $\leq$800 nm was required to retrieve the best axial resolution of the system, and to ensure a collection of at least 8 voxels per focal volume. The axial movement speed was limited by the electronic stage OSMS80-20ZF-0B (Sigma Koki, Tokyo, Japan), providing a maximum travel of up-to 1 mm/s.

In summary, we correlated the Nyquist-Shannon sampling theorem in laser-scanning multiphoton microscope to realize its impact over the field of view and its direct relationship with the excitation wavelength, laser repetition-rate, and fast-axis scanning frequency. We formulated a Nyquist figure-of-merit parameter to characterize a laser-scanning MPM in terms of its reliable digitization capability. We defined the maximum allowable FOV for such a system which must not be exceeded to prevent digital resolution loss. We defined a cross-over excitation wavelength, which must not be subceeded to prevent NFOM-constrained reduction to the optics-limited FOV.

Based on our derivation, we proposed the way to maximize an aliasing-free FOV yet not compromising with the imaging speed and/or the effective resolution by enabling a laser repetition-rate-limited maximized effective voxel-sampling rate. Remarkably, our idea contradicts the usage of a lower-pulse-rate laser

when a non-aliased extended FOV with a high enough lateral resolution and a fast-enough raster-scanning speed become the concerns.

We applied our idea in a custom built MPM with an FOV-resolution ratio of more than 3,000 and successfully demonstrated its optical-zoom-free submicron resolution retrieving ability by performing two-photon imaging of fine enough structures. We showed two-photon imaging above, near, and below the cross-over excitation wavelength, where, in the first two cases, the FOV remained optics-limited, whereas, in the last case, the FOV was rather constrained by NFOM.

This paper will help one to realize the consequences of the Nyquist-Shannon sampling theorem in the context of a laser-scanning multiphoton microscope. The Nyquist-exceeded mesoscopic imaging at submicron effective resolution presented in this paper will enable one to point-scan a large-volumetric sample, for instance, an intact whole mouse brain preserving an optics-limited resolution with a reduced requirement of digital image stitching, not to mention without employing an optical-zoom for high resolution retrieval. Apart from volumetric imaging, it further holds a tremendous potential for rapid giga-pixel imaging of large-area *ex-vivo* biopsy tissue-samples to enable a real-time visualization of fine submicron histopathological features without optical zooming.

Limitations of the study

The maximized square-shaped FOV demonstrated in this study is not suitable for those imaging applications which involve high frame-rate functional analysis. For such requirements, the slow-axis pixel number, and hence the slow-axis FOV can be easily reduced to boost the frame rate as described in *'Feasibility of high-frame-rate MPM imaging at maximized fast-axis FOV'*.

STAR★METHODS

Detailed methods are provided in the online version of this paper and include the following:

- KEY RESOURCES TABLE
- RESOURCE AVAILABILITY
  - Lead contact
  - Materials availability
  - Data and code availability
- EXPERIMENTAL MODEL AND SUBJECT DETAILS
- METHOD DETAILS
  - Mathematical formulation of the Nyquist-Shannon sampling theorem in a laser-scanning multiphoton microscope (MPM)
  - Construction of the mesoscopic laser-scanning MPM
  - Data processing and analysis
- QUANTIFICATION AND STATISTICAL ANALYSIS
- ADDITIONAL RESOURCES

SUPPLEMENTAL INFORMATION

Supplemental information can be found online at https://doi.org/10.1016/j.isci.2021.103041.

ACKNOWLEDGMENTS

This project was supported by Ministry of Science and Technology (Taiwan) with financial grants MOST 107-2221-E-002-157-MY3, MOST 107-2321-B-002-006, and MOST 110-2321-B-002-011. We thank Dr. Daniel Lin (SunJin Lab Co., Taiwan) for advice and support in sample preparation.

AUTHOR CONTRIBUTIONS

B. J. Borah designed, optimized and implemented the complete opto-electro-mechanical system, developed the C++ based control and data acquisition software, and further performed imaging experiments and data analysis. J.-C. Lee, H.-H. Chi, and C.-T. Yen were in charge for the preparation of the biological samples used in this study. Y.-T. Hsiao prepared the lower wavelength two-photon excitation source. C.-K. Sun initiated the concept and conducted the research. B. J. Borah and C.-K. Sun wrote the paper.

DECLARATION OF INTERESTS

The mesoscopic MPM is under national-phase patent applications through the Patent Cooperation Treaty (PCT), publication number: WO/2021/112942; a granted patent TWI714378B (Taiwan); inventors: C.-K. Sun & B. J. Borah; applicant: National Taiwan University, Taiwan. The compiled standalone acquisition software, being a part of the patent, will be available from the corresponding author upon reasonable request, for non-commercial use only, subject to regulation and approval from National Taiwan University, Taiwan.

Received: June 7, 2021
Revised: July 15, 2021
Accepted: August 23, 2021
Published: September 24, 2021

REFERENCES

Apolonski, A., Povazay, B., Unterhuber, A., Drexler, W., Wadsworth, W.J., Knight, J.C., and Russell, P.S.J. (2002). Spectral shaping of supercontinuum in a cobweb photonic-crystal fiber with sub-20-fs pulses. JOSA B *19*, 2165–2170.

Balu, M., Mikami, H., Hou, J., Potma, E.O., and Tromberg, B.J. (2016). Rapid mesoscale multiphoton microscopy of human skin. Biomed. Opt. Express *7*, 4375–4387.

Borah, B.J., and Sun, C.-K. (2021). A GPU-accelerated modified unsharp-masking method for high-frequency background-noise suppression. IEEE Access *9*, 68746–68757.

Borah, B.J., Chi, H.-H., Yen, C.-T., and Sun, C.-K. (2020). Super-speed multiphoton microscopy for mesoscopic volume imaging with ultra-dense sampling beyond Nyquist Limit. In Proc. SPIE 11245, Three-Dimensional and Multidimensional Microscopy: Image Acquisition and Processing XXVII, p. 1124515.

Bumstead, J.R., Park, J.J., Rosen, I.A., Kraft, A.W., Wright, P.W., Reisman, M.D., Côté, D.C., and Culver, J.P. (2018). Designing a large field-of-view two-photon microscope using optical invariant analysis. Neurophoton *5*, 025001.

Chakraborty, S., Lee, S.Y., Lee, J.C., Yen, C.T., and Sun, C.K. (2019). Saturated two-photon excitation fluorescence microscopy for the visualization of cerebral neural networks at millimeters deep depth. J. Biophotonics *12*, e201800136.

Charan, K., Li, B., Wang, M., Lin, C.P., and Xu, C. (2018). Fiber-based tunable repetition rate source for deep tissue two-photon fluorescence microscopy. Biomed. Opt. Express *9*, 2304–2311.

Chen, W.N., Lee, C.H., Lin, S.H., Wong, C.W., Sun, W.H., Wood, J.N., and Chen, C.C. (2014). Roles of ASIC3, TRPV1, and NaV1. 8 in the transition from acute to chronic pain in a mouse model of fibromyalgia. Mol. pain *10*, 1744–8069.

Chun, W., Do, D., and Gweon, D.G. (2013). Design and demonstration of multimodal optical scanning microscopy for confocal and two-photon imaging. Rev. Sci. Instrum. *84*, 013701.

Chung, K., and Deisseroth, K. (2013). CLARITY for mapping the nervous system. Nat. Methods *10*, 508–513.

Denk, W., Strickler, J.H., and Webb, W.W. (1990). Two-photon laser scanning fluorescence microscopy. Science *248*, 73–76.

Drobizhev, M., Makarov, N.S., Tillo, S.E., Hughes, T.E., and Rebane, A. (2011). Two-photon absorption properties of fluorescent proteins. Nat. Methods *8*, 393–399.

Gil, H.H., Golgher, L., Israel, S., Kain, D., Cheshnovsky, O., Parnas, M., and Blinder, P. (2018). PySight: plug and play photon counting for fast continuous volumetric intravital microscopy. Optica *5*, 1104–1112.

Haji-Saeed, B., Khoury, J., Woods, C.L., Pyburn, D., Sengupta, S.K., and Kierstead, J. (2007). Mapping approach for image correction and processing for bidirectional resonant scanners. Opt. Eng. *46*, 027007.

Heintzmann, R., and Sheppard, C.J.R. (2007). The sampling limit in fluorescence microscopy. Micron *38*, 145–149.

Helmchen, F., and Denk, W. (2005). Deep tissue two-photon microscopy. Nat. Methods *2*, 932–940.

Horton, N.G., and Xu, C. (2015). Dispersion compensation in three-photon fluorescence microscopy at 1,700 nm. Biomed. Opt. Express *6*, 1392–1397.

Horton, N.G., Wang, K., Kobat, D., Clark, C.G., Wise, F.W., Schaffer, C.B., and Xu, C. (2013). In vivo three-photon microscopy of subcortical structures within an intact mouse brain. Nat. Photon *7*, 205–209.

Hsiao, Y.T., Huang, Y.F., Borah, B.J., Chen, S.K., and Sun, C.K. (2021). Single-laser-based simultaneous four-wavelength excitation source for femtosecond two-photon fluorescence microscopy. Biomed. Opt. Express *12*, 4661–4679.

Jacques, S.L. (2013). Optical properties of biological tissues: a review. Phys. Med. Biol. *58*, 37–61.

Jaepel, J., Hübener, M., Bonhoeffer, T., and Rose, T. (2017). Lateral geniculate neurons projecting to primary visual cortex show ocular dominance plasticity in adult mice. Nat. Neurosci. *20*, 1708–1714.

Kobat, D., Durst, M.E., Nishimura, N., Wong, A.W., Schaffer, C.B., and Xu, C. (2009). Deep tissue multiphoton microscopy using longer wavelength excitation. Opt. Express *17*, 13354–13364.

Kong, L., Tang, J., Little, J.P., Yu, Y., Lämmermann, T., Lin, C.P., Germain, R.N., and Cui, M. (2015). Continuous volumetric imaging via an optical phase-locked ultrasound lens. Nat. Methods *12*, 759–762.

Li, B., Wu, C., Wang, M., Charan, K., and Xu, C. (2020). An adaptive excitation source for high-speed multiphoton microscopy. Nat. Methods *17*, 163–166.

Liang, X., Hu, W., and Fu, L. (2010). Pulse compression in two-photon excitation fluorescence microscopy. Opt. Express *18*, 14893–14904.

Mütze, J., Iyer, V., Macklin, J.J., Colonell, J., Karsh, B., Petrášek, Z., Schwille, P., Looger, L.L., Lavis, L.D., and Harris, T.D. (2012). Excitation spectra and brightness optimization of two-photon excited probes. Biophysical J. *102*, 934–944.

Naik, S.K., and Murthy, C.A. (2003). Hue-preserving color image enhancement without Gamut problem. IEEE Trans. Image Process. *12*, 1591–1598.

Nassar, M.A., Stirling, L.C., Forlani, G., Baker, M.D., Matthews, E.A., Dickenson, A.H., and Wood, J.N. (2004). Nociceptor-specific gene deletion reveals a major role for Nav1. 7 (PN1) in acute and inflammatory pain. Proc. Natl. Acad. Sci. *101*, 12706–12711.

Ntziachristos, V. (2010). Going deeper than microscopy: the optical imaging frontier in biology. Nat. Methods *7*, 603–614.

Nyquist, H. (1928). Certain topics in telegraph transmission theory. Trans. AIEE *47*, 617–644.

Pawley, J.B. (2006). In Handbook of Biological Confocal Microscopy, J.B. Pawley, ed. (Springer), pp. 59–79.

Prevedel, R., Verhoef, A.J., Pernía, A.J., Weisenburger, S., Huang, B.S., Nöbauer, T., Fernández, A., Delcour, J.E., Golshani, P., Baltuska, A., and Vaziri, A. (2016). Fast volumetric calcium imaging across multiple cortical layers using sculpted light. Nat. Methods *13*, 1021–1028.

Reza, A.M. (2004). Realization of the contrast limited adaptive histogram equalization (CLAHE)

for real-time image enhancement. J. VLSI Signal Processing-Systems Signal, Image, Video Technology *38*, 35–44.

Rosenegger, D.G., Tran, C.H.T., LeDue, J., Zhou, N., and Gordon, G.R. (2014). A high performance, cost-effective, open-source microscope for scanning two-photon microscopy that is modular and readily adaptable. PLoS One *9*, e110475.

Shannon, C.E. (1949). Communications in the presence of noise. Proc. IRE *37*, 10–21.

Sheppard, C., and Gu, M. (1990). Image formation in two-photon fluorescence microscopy. Optik *86*, 104–106.

Sofroniew, N.J., Flickinger, D., King, J., and Svoboda, K. (2016). A large field of view two-photon mesoscope with subcellular resolution for in vivo imaging. eLife *5*, e14472.

Stirman, J.N., Smith, I.T., Kudenov, M.W., and Smith, S.L. (2016). Wide field-of-view, multi-region, two-photon imaging of neuronal activity in the mammalian brain. Nat. Biotechnol. *34*, 857–862.

Sun, C.-K., and Borah, B.J. (2019). Large-angle Optical Raster Scanning System for Deep Tissue Imaging. U.S. Patent Application No. 20210173189(A1) (U.S. Patent and Trademark Office).

Terada, S.I., Kobayashi, K., Ohkura, M., Nakai, J., and Matsuzaki, M. (2018). Super-wide-field two-photon imaging with a micro-optical device moving in post-objective space. Nat. Commun *9*, 3550.

Theer, P., Hasan, M.T., and Denk, W. (2003). Two-photon imaging to a depth of 1000 μm in living brains by use of a Ti:Al2O3 regenerative amplifier. Opt. Lett. *28*, 1022–1024.

Tsai, P.S., Mateo, C., Field, J.J., Schaffer, C.B., Anderson, M.E., and Kleinfeld, D. (2015). Ultra-large field-of-view two-photon microscopy. Opt. Express *23*, 13833–13847.

Virtue, P., and Lustig, M. (2017). The empirical effect of Gaussian noise in undersampled MRI reconstruction. Tomography *3*, 211–221.

Weisenburger, S., Tejera, F., Demas, J., Chen, B., Manley, J., Sparks, F.T., Traub, F.M., Daigle, T., Zeng, H., Losonczy, A., and Vaziri, A. (2019). Volumetric Ca2+ imaging in the mouse brain using hybrid multiplexed sculpted light microscopy. Cell *177*, 1050–1066.

Westberg, K.G., and Kolta, A. (2011). The trigeminal circuits responsible for chewing. Int. Rev. Neurobiol. *97*, 77–98.

Xiao, S., and Mertz, J. (2019). Contrast improvement in two-photon microscopy with instantaneous differential aberration imaging. Biomed. Opt. Express *10*, 2467–2477.

Zipfel, W.R., Williams, R.M., and Webb, W.W. (2003). Nonlinear magic: multiphoton microscopy in the biosciences. Nat. Biotechnol. *21*, 1369–1377.

STAR★METHODS

KEY RESOURCES TABLE

REAGENT or RESOURCE	SOURCE	IDENTIFIER
Antibodies		
Rabbit anti-GFP	ThermoFisher	Cat# A-11122; RRID: AB_221569
Goat-anti-Rabbit-Alexa 546	ThermoFisher	Cat# A-11035; RRID: AB_2534093
Chemicals, peptides, and recombinant proteins		
RapiClear CS solution	SunJin Lab Co.	Cat# RCCS002
RapiClear 1.52	SunJin Lab Co.	Cat# RC152002
40% acrylamide solution	Bio-Rad Laboratories, Inc.	Cat# 161-0140
2% bis-acrylamide solution	Bio-Rad Laboratories, Inc.	Cat# 161-0142
16% paraformaldehyde	Electron Microscopy Sciences	Cat# 15710
VA-044 photoinitiator	FUJIFILM Wako Pure Chemical Corporation	Cat# VA-044
sodium dodecyl sulfate (SDS)	Sigma-Aldrich	Cat# L3771-1KG
Triton X-100	ThermoFisher	Cat# 28313
Experimental models: organisms/strains		
Mouse: Thy1-GFP line M	The Jackson Laboratory	JAX: 007788
Mouse: Nav1.8-cre	Nassar et al., 2004 Chen et al., 2014	MGI: 3053096
Mouse: Ai14	The Jackson Laboratory	JAX: 007908
Software and algorithms		
ImageJ	National Institutes of Health, USA	https://imagej.nih.gov/ij/
OpenCV	Intel Corporation, USA	https://opencv.org/
Amira	Thermo Fisher Scientific	https://www.fei.com/software/amira-3d-for-life-sciences/
Matlab	MathWorks, USA	https://www.mathworks.com/
Origin	OriginLab, USA	https://www.originlab.com/
Other		
iSpacer	SunJin Lab Co.	Cat# IS011

RESOURCE AVAILABILITY

Lead contact

Further information and requests for resources should be directed to and will be fulfilled by the lead contact, Chi-Kuang Sun (sun@ntu.edu.tw).

Materials availability

This study did not generate new unique reagents.

Data and code availability

- The data/images generated and/or analyzed to support the findings of our study are presented in the paper, STAR Methods, and supplemental information. More details are available from the lead contact upon reasonable request.
- This paper does not report original code.
- Any additional information required to reanalyze the data reported in this paper is available from the lead contact upon request.

EXPERIMENTAL MODEL AND SUBJECT DETAILS

Two transgenic thy1-GFP and one Nav1.8-tdTomato male mice used in this study were 8-week-old. The thy1-GFP mice were purchased from the Jackson Laboratory (JAX: 007788). The Nav1.8-tdTomato mice were the offspring produced by crossing Ai14 (JAX: 007908) and Nav1.8-cre mice (MGI: 3053096, http://www.informatics.jax.org/allele/MGI:3053096; Nassar et al., 2004; Chen et al., 2014). The mice were housed with a 12-hour light/12-hour dark cycle and fed ad libitum. They were maintained in accordance with guidelines approved in the Codes for Experimental Use of Animals of the Council of Agriculture of Taiwan, based on the Animal Protection Law of Taiwan.

For the sample preparation, mice were processed with passive CLARITY method (Chung and Deisseroth, 2013). The mice were anesthetized with overdose of sodium pentobarbital (100 mg/kg) and perfused transcardially with ice-cold phosphate buffered saline, and followed with hydrogel monomer solution (4% acrylamide, 2% bis-acrylamide, 4% paraformaldehyde and VA-044 initiator). The brains and sciatic nerves with dorsal root ganglion were dissected and incubated in the hydrogel monomer solution at 4°C for 2 days, and then polymerized at 37°C for 3 hours. After removing the extra hydrogel from the surface, the brain and nerve samples were washed on a rotating shaker with 4% sodium dodecyl sulfate (SDS) clearing solution at room temperature. The clearing solution was replaced each week and the tissue clearing status was monitored. The passive CLARITY clearing procedure was performed 4 months for the whole-brain clarifying samples, while one week was enough for the sciatic nerve sample. After the passive CLARITY clearing procedure, the brain samples were washed in PBST (0.3% Triton X-100 in phosphate buffered saline) for 3 days to remove the SDS clearing solution. The medulla was then sliced by a vibratome into 500 μm sections. We used the RapiClear CS (refractive index 1.45; SunJin Lab Co., Taiwan) for refractive index matching overnight, and then embedded the medulla sample, whole-brain sample, and nerve sample within suitable spacers (iSpacer; SunJin Lab Co., Taiwan) for imaging.

For immunohistochemical staining, two thy1-GFP mice were first transcardially perfused with ice-cold phosphate buffered saline and followed with 4% paraformaldehyde. The brains were dissected and post-fixed at 4°C for 2 days. The 250 μm sections were prepared by a vibratome in sagittal or coronal orientation. The sections were stained with immunohistochemistry procedures: rabbit anti-GFP antibody (ThermoFisher, A-11122, 1:200), Goat-anti-Rabbit-Alexa 546 (ThermoFisher, A-11035, 1:400). The sections were then processed with RapiClear 1.52 (SunJin Lab Co., Taiwan) for refractive index matching.

METHOD DETAILS

Mathematical formulation of the Nyquist-Shannon sampling theorem in a laser-scanning multiphoton microscope (MPM)

According to the Nyquist-Shannon sampling theorem, while digitizing an analog signal, to reliably reconstruct it from the digitized data points, the interval between the intensity measurements must be less than or equal to half of the highest frequency present in the analog signal (Nyquist, 1928; Shannon, 1949; Pawley, 2006; Heintzmann and Sheppard, 2007). In case of a digital imaging system, the size of each pixel in the digitized image must be at least half of the optics-limited resolution provided by the system,

$$\text{i.e., } d \leq \frac{1}{2} r^{FWHM}, \qquad \text{(Equation S1)}$$

where d is the pixel size and r^{FWHM} is the optical lateral resolution (Zipfel et al., 2003; Sheppard and Gu, 1990) which is represented as

$$r^{FWHM} = \begin{cases} \dfrac{0.532\ \lambda_{exc}}{\sqrt{n}\,NA}, & NA \leq 0.7 \\ \dfrac{0.541\ \lambda_{exc}}{\sqrt{n}\,NA^{0.91}}, & NA > 0.7 \end{cases}, \qquad \text{(Equation S2)}$$

where λ_{exc}, n, and NA stand for excitation wavelength, order of the multiphoton process, and numerical aperture of the objective lens, respectively.

Considering Equation (S1), for a fast-axis field of view of FOV_{max}, the minimum required pixel number P_n can be given as

$$P_n = \frac{FOV_{max}}{d} = \frac{2\ FOV_{max}}{r^{FWHM}}. \quad \text{(Equation S3)}$$

For a resonant scanner with a scanning frequency of f, the line-frequency or the line-rate is essentially $2f$. Now, presuming a constant scan velocity along the fast-axis, the minimum effective voxel-sampling rate V_{min} to fulfil the Nyquist criterion can be expressed as

$$V_{min} = \frac{4\ f\ FOV_{max}}{r^{FWHM}}. \quad \text{(Equation S4)}$$

For a multiphoton microscopy system, for efficient nonlinear excitation, a pulsed laser source is typically utilized to achieve a high enough pulse energy. Following Equation (S4), the required repetition-rate (R) of the pulsed laser source would thus be

$$R \geq V_{min}\ N, \quad \text{(Equation S5)}$$

where N is an integer signifying number of optical pulse(s) per voxel, presuming a synchronized sampling to the laser optical pulses.

Using Equation (S2), for a general laser-scanning MPM, V_{min} can be represented as

$$V_{min} = \begin{cases} \frac{7.5188\sqrt{n}\ NA\ f\ FOV_{max}}{\lambda_{exc}}, & NA \leq 0.7 \\ \frac{7.3937\sqrt{n}\ NA^{0.91}\ f\ FOV_{max}}{\lambda_{exc}}, & NA > 0.7 \end{cases}. \quad \text{(Equation S6)}$$

Considering N = 1 in Equation (S5) for the optimized case, the minimum laser repetition-rate required will be

$$R_{min} = V_{min}. \quad \text{(Equation S7)}$$

To characterize a laser-scanning MPM in terms of its optical-resolution retrieving ability, a Nyquist figure-of-merit (NFOM) expression can be formulated as

$$NFOM = \frac{V_{eff}}{V_{min}}, \quad \text{(Equation S8)}$$

where V_{eff} is the effective voxel-sampling rate of the system. In case of pulse-level synchronization, V_{eff} can be replaced with R/N, and thus substituting V_{eff} and V_{min}, Equation (S8) can be written as

$$NFOM = \begin{cases} \frac{0.133\ R\ \lambda_{exc}}{\sqrt{n}\ N\ f\ NA\ FOV_{max}}, & NA \leq 0.7 \\ \frac{0.1353\ R\ \lambda_{exc}}{\sqrt{n}\ N\ f\ NA^{0.91}\ FOV_{max}}, & NA > 0.7 \end{cases}. \quad \text{(Equation S9)}$$

Using Equation (S9), for an optimized condition with NFOM = 1 and N = 1, the maximum achievable aliasing-free FOV for a specified set of laser, fast-axis scanner, and objective lens can be estimated as

$$FOV_{max} = \begin{cases} \frac{0.133\ R\ \lambda_{exc}}{\sqrt{n}\ f\ NA}, & NA \leq 0.7 \\ \frac{0.1353\ R\ \lambda_{exc}}{\sqrt{n}\ f\ NA^{0.91}}, & NA > 0.7 \end{cases}. \quad \text{(Equation S10)}$$

For a conventional laser-scanning system (Chun et al., 2013), the optics-limited fast-axis field of view, FOV_{OL} can be determined as

$$FOV_{OL} = 2\tan|\theta_{\pm}| \times \frac{f_o\ f_s}{f_t}, \quad \text{(Equation S11)}$$

where $\theta_{\pm}$ is the fast-axis scan-angle by the scanning mirror with respect to the optical axis, f_o, f_s, and f_t are effective focal lengths of the objective lens, scan lens, and tube lens, respectively. Thus, considering Equations (S6), (S7), and (S11), V_{min} and R_{min} for a conventional laser-scanning MPM can be estimated as

$$V_{min} = R_{min} = \begin{cases} \dfrac{15.0376\sqrt{n}\ NA\ f\ \tan|\theta_{\pm}|\ f_o\ f_s}{\lambda_{exc}\ f_t}, & NA \leq 0.7 \\ \dfrac{14.7874\sqrt{n}\ NA^{0.91}\ f\ \tan|\theta_{\pm}|\ f_o\ f_s}{\lambda_{exc}\ f_t}, & NA > 0.7 \end{cases}. \quad \text{(Equation S12)}$$

Following Equation (S10), for a laser-scanning MPM with $FOV_{OL} \leq FOV_{max}$, a cross-over excitation wavelength λ_c can be formulated as

$$\lambda_c = \begin{cases} \dfrac{7.5188\sqrt{n}\ f\ NA\ FOV_{OL}}{R}, & NA \leq 0.7 \\ \dfrac{7.3937\ \sqrt{n}\ f\ NA^{0.91}\ FOV_{OL}}{R}, & NA > 0.7 \end{cases}. \quad \text{(Equation S13)}$$

Considering a polygon-scanning system for the fast-axis, with F and RPM to be the number of facets and revolutions per minute for the same, respectively, Equations (S6), (S9), (S10), and (S13) can be further extended as follows

$$V_{min} = \begin{cases} \dfrac{0.0627\sqrt{n}\ NA\ \ F\ \ RPM\ \ FOV_{max}}{\lambda_{exc}}, & NA \leq 0.7 \\ \dfrac{0.0616\sqrt{n}\ NA^{0.91}\ F\ \ RPM\ \ FOV_{max}}{\lambda_{exc}}, & NA > 0.7 \end{cases}, \quad \text{(Equation S14)}$$

$$NFOM = \begin{cases} \dfrac{15.96\ R\ \lambda_{exc}}{\sqrt{n}\ \ N\ \ F\ \ RPM\ \ NA\ \ FOV_{max}}, & NA \leq 0.7 \\ \dfrac{16.23\ R\ \lambda_{exc}}{\sqrt{n}\ \ N\ \ F\ \ RPM\ \ NA^{0.91}\ FOV_{max}}, & NA > 0.7 \end{cases}, \quad \text{(Equation S15)}$$

$$FOV_{max} = \begin{cases} \dfrac{15.96\ R\ \lambda_{exc}}{\sqrt{n}\ \ F\ \ RPM\ \ NA}, & NA \leq 0.7 \\ \dfrac{16.23\ R\ \lambda_{exc}}{\sqrt{n}\ \ F\ \ RPM\ \ NA^{0.91}}, & NA > 0.7 \end{cases}, \quad \text{(Equation S16)}$$

$$\lambda_c = \begin{cases} \dfrac{0.0627\sqrt{n}\ \ F\ \ RPM\ \ NA\ FOV_{OL}}{R}, & NA \leq 0.7 \\ \dfrac{0.0616\ \sqrt{n}\ \ F\ \ RPM\ \ NA^{0.91}\ FOV_{OL}}{R}, & NA > 0.7 \end{cases}, \quad \text{(Equation S17)}$$

where the line rate, i.e., two times the resonant scanner frequency ($2f$) was substituted with $\frac{F \times RPM}{60}$.

Construction of the mesoscopic laser-scanning MPM

Design and performance analysis of a large angle optical raster scanning (LAORS) system. Figure S1A depicts the essential elements of a large-angle optical raster scanning (LAORS) system. A pulsed laser source (Fidelity-2 fiber laser; Coherent, Inc., CA, USA) centered around 1,070 nm, producing <60 femtosecond pulses at 70 MHz repetition-rate was used as the primary source for nonlinear excitation. A resonant scanner (CRS 4 kHz, driver: 311-149887) for fast X axis and a galvanometer scanner (8320K, driver: MicroMax 671) for slow Y axis (both from Cambridge Technology, MA, USA) were utilized for raster scanning. A dedicated tube lens was custom designed combining three plano-convex lenses (Edmund Optics: 86-925), each with clear aperture and EFL of 73.5 mm and 500 mm, respectively, resulting in a combined EFL of 166.7 mm. The custom tube lens was optically coupled to a general scan lens (LSM05-BB, Thorlabs, NJ, USA) with an EFL of 110 mm, and a 0.95 NA, 20× objective lens (Olympus XLUMPlanFI, 20×/0.95W) with an EFL of 9 mm.

Following Equation (S11), for a fast-axis FOV of 1.6 mm, the LAORS system requires a fast-X-axis scanning angle of $\sim \pm 7.7°$ with respect to the optical axis. Being a symmetrical system, the same scanning angle is required for a ~1.6 mm slow-Y-axis FOV. The optimization of the system was based on an optical simulation by means of a ray tracing software (Radiant Zemax, USA). We simultaneously rendered 0° and $\pm 7.7°$ off-axis configurations (over the scan lens) in X and Y directions by the resonant and galvanometer scanning mirrors, respectively, at a wavelength λ = 1,070 nm and considering the objective lens as a paraxial lens (perfect lens) with EFL = 9 mm. With an input beam of 9.25 mm in diameter, the root mean square (RMS) wavefront errors (without defocus) and Strehl Ratios were found to be $<0.07\lambda$ and >80%, respectively,

for 0° and ±7.7° off-axis configurations, indicating a diffraction-limited performance up-to the edges of the FOV (Maréchal criterion). Figures S2A–S2C depict modulus of the optical transfer function (OTF) versus spatial frequency (cycles/mm) for angles (over the scan lens) of ±7.7° off-axis in the X direction, 0° off-axis in X and Y directions, and ±7.7° off-axis in the Y direction, respectively. It is observed that both the spatial frequency and contrast remain adequate from the center up-to the edges of the square-shaped FOV. In addition, the RMS wavefront errors (without defocus) were evaluated simultaneously for all the above configurations of ±7.7° off-axis in the X & Y directions (FOV-edges), and 0° off-axis in X & Y directions (FOV-center) over the scan lens at a single focal plane (adjusted once), and were found to be under 0.1λ at all these locations without any further adjustment to the focal plane.

While designing the LAORS system, we optimized the parameters at a central wavelength of 1,070 nm. Since our multiple wavelength studies were not simultaneously performed, the issue of chromatic aberration did not become a primary concern for us. While shifting to a different wavelength a minor adjustment to the axial-axis was enough to find the focal plane. Note that in our optical simulation the objective lens was treated to be a perfect lens due to unavailability of internal optical details, and hence the practical performance of the system might vary. Referring to Figure S3, the effective lateral and axial resolutions in the central imaging-area were around 0.483 ± 0.034 μm and 2 ± 0.3 μm, respectively for a 1,070 nm central excitation wavelength. With a limited field number, an objective lens induces vignetting effect at larger scanning angles, i.e., towards the FOV-corners. In addition, due to increased optical aberrations, the performance at FOV-corners and FOV-edges does not persist under the diffraction limit. Employing an adaptive optics system and/or utilizing custom manufactured optical components together with a high field number objective lens can further improve the optical performance. Additionally, due to such optical aberrations as well as vignetting effects, the pixels do encounter non-uniform intensity across the large FOV as a result of lower excitation efficiency towards the edges. For a fixed-power excitation scenario, a dynamic PMT-gain adjustment can be applied so as to boost/reduce the pixel intensity dynamically across the FOV to compensate for the non-uniform excitation efficiency. Likewise, a contrast limited adaptive histogram equalization (CLAHE) (Reza, 2004) can be helpful to improve the same. In the context of SNR, our recently published high-frequency noise suppression method (Borah and Sun, 2021) can further help improve the MPM-image fidelity.

Design of fluorescence collecting optics. Figure S1B illustrates the fluorescence collecting optics, an essential part of the LAORS system. The emerging fluorescence signal is collected by the high-NA and low magnification objective lens and is reflected toward the detection unit by a dichroic beam-splitter (FF801-Di02, Semrock, for 1,070 nm excitation, or FF735-Di02, Semrock, for 919 nm and 824 nm excitations). The detection unit comprises a relay system with demagnification factor of 3.75 achieved by two lenses with EFLs of 150 mm (Edmund Optics: 32-982) and 40 mm (Edmund Optics: 48-654), respectively, thereby resulting in a 4 mm focused spot diameter throughout the scanning range, i.e., small enough to be inside photosensitive area of the PMT (R10699, Hamamatsu Photonics, Japan; photosensitive area = 24 × 8 mm^2). A band-pass filter (FF01-580/60-25-D, Semrock) and a colored glass filter (FGB37-A, Thorlabs) were placed prior to the PMT photocathode to ensure detection of two-photon fluorescence signal from the Nav1.8-tdTomato or Alexa Fluor 546 samples. Likewise, another band-pass filter (FF03-525/50-25, Semrock) and the same colored glass filter were used to ensure detection of thy1-GFP two-photon fluorescence signal.

Tuning of excitation wavelength. The Fidelity-2 fiber laser produced <60 fs pulses at a center-wavelength of around 1,070 nm, which was optically coupled to a 7 mm-long photonic crystal fiber to introduce a negative dispersion for self-phase modulation-enabled spectral broadening (Hsiao et al., 2021), so as to obtain the lower excitation wavelengths required for the Alexa Fluor 546 and Thy1-GFP related experiments. A half-wave plate was added prior to the fiber-coupling system to enable spectrum-shaping by means of polarization rotation (Apolonski et al., 2002). We applied a long-pass filter cut-on at 750 nm and a short-pass filter cut-off at 850 nm to enable a spectrum centered around 824 nm for Alexa Fluor 546 excitation (Mütze et al., 2012), and the same long-pass filter with a short-pass filter cut-off at 1,000 nm to allow a spectrum centered around 919 nm for Thy1-GFP excitation (Drobizhev et al., 2011). A grating-pair for pulse pre-chirping (Liang et al., 2010) was finally utilized to make pulse durations at the focal point of the objective lens shorter than 60 fs in each case.

Construction of data acquisition system to enable NFOM ≥ 1. Figure S4 depicts the block diagram of the developed control and data acquisition system. A digitizer ATS9440 (Alazar Technologies Inc., Canada)

was used for digitization up-to a sampling rate of 125 Mega Samples per second (MSps) for up-to 4 parallel channels. A multifunction I/O card PCIe-6341 (National Instruments Corporation, TX, USA) was utilized for synchronization of slow Y axis with fast X axis. A sawtooth waveform was generated and applied to the galvanometer scanning mirror driver via PCIe-6341. The slow-axis movement was precisely controlled by the software and did not encounter any distortion. However, the resonant scanning mirror indeed produces nonlinear distortions due to acceleration and deceleration of the fast-scanning mirror. To get a uniform FOV, we employed real-time remapping of the digitized data following a prior idea reported by Haji-Saeed et al. (2007). Based on the cosinusoidal motion of the resonant scanning mirror, the C++ based software rearranged the acquired samples (digitized by ATS9440) utilizing NVIDIA's compute unified device architecture (CUDA) acceleration before generating the 8-bit raw images. The developed data acquisition system holds a capability of simultaneously sampling 4 channels at up-to 125 MSps sampling rate, reaching a single-frame pixel number of 15,720 × 16,000 for each of the 4 channels, leading to a total of ~1 Gigapixels per frame, while maintaining ~0.5 fps; including calibration, preview, and storage of the acquired data.

The LAORS system was designed to yield an FOV of up-to 1.6 × 1.6 mm^2. Following Equations (3) or (6), for two-photon imaging at 1,070 nm excitation with a 0.95 NA objective lens while employing a 4 kHz resonant scanner, we required $R_{min} = 59.7$ MHz for $FOV_{OL} = 1.6$ mm $= FOV_{max}$. To achieve the same, we opted for the 70 MHz femtosecond laser with ~1,070 nm central wavelength. Following Equation (4) with N = 1 for repetition-rate-limited maximized voxel-sampling rate, the Nyquist figure-of-merit is evaluated to be around 1.17, indicating a Nyquist-exceeded aliasing-free acquisition.

By means of the ultra-high effective voxel-sampling rate of 70 M/s, we obtained a pixel number of 8,800 in each fast-axis line with a sampling spacing of ~182 nm. For synchronization, we connected the 70 MHz sync signal output from the Fidelity-2 fiber laser into the external clock input of the digitizer ATS9440, and taking advantage of the dual-port memory supported by ATS9440, we developed the C++ codes for real-time multi-channel acquisition. To maintain the same sampling spacing of ~182 nm vertically, we scanned 8,800 lines along the slow Y axis. Thus, exceeded the Nyquist-Shannon criterion identically in both X and Y axes at the same time, with an ability of scanning a ~1.6 × 1.6 × 1.6 mm^3 volume with 8,800 × 8,800×2000 (× 4 channels), i.e., ~619.5 Giga-voxels in total within <39 min at 0.8 μm Z-step, and maintaining Nyquist-exceeded voxel size, volume-scanning speed, and line-scanning speed of <0.027 μm^3, >1750 μm^3/ms, and >12 mm/ms, respectively, while maintaining an effective pixel dwell time of <40 ns, at up-to an effective lateral resolution of <500 nm. Maintaining this data acquisition speed, the mesoscopic MPM holds the capability of scanning a ~500 mm^3 intact whole mouse brain sample within <2 days with ~0.5 μm^3 two-photon effective 3D resolution, maintaining a Nyquist-satisfied voxel size of 0.182 × 0.25 × 1 μm^3. In this manuscript with a focus on NFOM only, we demonstrated single-channel operation of the system.

The bandwidth of the data acquisition system was limited by a transimpedance amplifier (C6438-01, Hamamatsu Photonics, Japan) used for current to voltage conversion of the photomultiplier tube (PMT) output signal. Another issue we encountered is that while implementing bi-directional scanning, the digitizer does not look for the odd-line trigger events when it is busy acquiring the pre-defined number of samples in the preceding even-line. As a remedy, we set the number of samples per line in a way that sampling events for each line always finishes before occurrence of the next line trigger. While doing so, we had to sacrifice a few tens of microns from the extended millimeter-scale FOV.

The C++ based control and data acquisition software was developed using Microsoft Visual Studio 2017 (Microsoft Corporation, Redmond, WA, USA) which utilized AlazarTech C/C++ application program interface (API) (version: 6.7.0) and NI-DAQmx C API (version: 19.1). Taking advantage of dual-port memory supported by ATS9440, we enabled simultaneous data transfer to the host memory during ongoing data acquisition (without frame-rate drop). For high-speed data processing, NVIDIA's CUDA (version: 10.1) accelerated C/C++ based OpenCV (version: 4.1.1) was utilized. Table S1 enlists the prerequisites for the control and data acquisition software. Table 2 illustrates the acquisition capability of the data acquisition system at various sampling rates in terms of pixel numbers, data sizes, and frame rates.

The software further implicated a multithreaded control algorithm for synchronization of slow Y axis with fast X axis, without sending an external electrical frame-trigger signal after completion of each frame. A 16-bit digital to analog converter (DAC) module (Model: 6757; Cambridge Technology, MA, USA) was

interfaced with the driver module for galvanometer scanning mirror (MicroMax 671; Cambridge Technology, MA, USA) for achieving a 16-bit precision movement along the slow Y axis. To send the 16-bit binary data words to the 6757 DAC module, we utilized the PCIe-6341 (with 24 digital I/O pins) which was directly interfaced to the computer motherboard; enabling a direct control over the slow Y axis from the master C++ program. A background high-priority thread was used to continuously monitor the line trigger events from the resonant scanning mirror driver, and to produce the 16-bit data words (generating a sawtooth waveform), i.e., the angle-positioning-steps to the DAC module making use of 16-bit precision. We successfully reached a frame-rate of up-to ~980 fps with single-frame pixel number of 15,720 × 8 (×4 channels), i.e., 125,760 (×4 channels) voxels per frame at a sampling rate of 125 MSps.

Data processing and analysis

We applied CLAHE (Reza, 2004) to the maximal intensity projected images presented in Figures 2D–2G and Figures 5A and 5C with a maximum slope of 3 using ImageJ standard function. To not alter the color-coding information, we first converted the images from RGB to HSV and applied the algorithm in the value channel only (Naik and Murthy, 2003) so as to preserve the hue and saturation channels. Finally, HSV images were converted back to RGB. CUDA-accelerated C/C++ based OpenCV standard functions were utilized for the RGB and HSV conversions. Grayscale images of thin sections shown in Figures 2J–2N and Figures 3A–C, 3E–G were Z-projected (average-intensity) using ImageJ. Contrast-adjustment was performed globally in the full-FOV image before digitally zooming (cropping and enlarging) the same for performing the resolution analysis in each case. Enlarged images in Figures 2L–2N depict the worst-case undersampled scenarios which were obtained from the original image in Figure 2K using OpenCV. For the 3D-rendering results presented in Figures 2A–2C and Figures 5D–5F, due to graphics memory limitation, we downscaled the images by 4-times to reduce data-size. Intensity profiles shown in Figures 2 and 3 were obtained using ImageJ. MATLAB R2016b was used to simulate and plot the graphs presented in Figure 1. OriginPro was used for plotting all other graphs.

QUANTIFICATION AND STATISTICAL ANALYSIS

Means and/or standard deviations related to SNR, SBR, and contrast ratio measurements in Figure 4 were obtained using ImageJ standard functions. In Figure S3, effective two-photon resolution was obtained considering cross sections of multiple microspheres as illustrated in Figure S3 legend, where an error bar denotes standard deviation.

ADDITIONAL RESOURCES

Experimental protocols were approved by the Institutional Animal Care and Use Committee of National Taiwan University, Taipei, Taiwan (approval number: NTU105-EL-00113).